Impact of momentum perturbation on convective boundary layer turbulence

Mukesh Kumar[1,4,*], Alex Jonko[1], William Lassman[2], Jeffrey D. Mirocha[2], Branko Kosović[3], and Tirtha Banerjee[4]

[1]Los Alamos National Laboratory, NM, USA
[2]Lawrence Livermore National Laboratory, CA, USA
[3]National Center for Atmospheric Research, CO, USA
[4]Department of Civil and Environmental Engineering, University of California, Irvine, CA, USA
[*]Correspondence to: Mukesh Kumar, mukeshk@uci.edu

January, 2022

Abstract

Mesoscale-to-microscale coupling is an important tool to conduct turbulence-resolving multiscale simulations of realistic atmospheric flows, which are crucial for applications ranging from wind energy to wildfire spread studies. Different techniques are used to facilitate the development of realistic turbulence in the large-eddy simulation (LES) domain while minimizing computational cost. Here, we explore the impact of a simple and computationally efficient Stochastic Cell Perturbation method using momentum perturbation (SCPM-M) to accelerate turbulence generation in boundary-coupled LES simulations using the Weather Research and Forecasting (WRF) model. We simulate a convective boundary layer (CBL) to characterize the production and dissipation of turbulent kinetic energy (TKE) and the variation of TKE budget terms. Furthermore, we evaluate the impact of applying momentum perturbations of three magnitudes below, up to, and above the CBL on the TKE budget terms. Momentum perturbations greatly reduce the fetch associated with turbulence generation. When applied to half the vertical extent of the boundary layer, momentum

perturbations produce an adequate amount of turbulence. However, when applied above the CBL, additional structures are generated at the top of the CBL, near the inversion layer. The magnitudes of the TKE budgets produced by SCPM-M when applied at varying heights and with different perturbation amplitudes are always higher near the surface and inversion layer than those produced by No-SCPM, as are their contributions to the TKE. This study provides a better understanding of how SCPM-M reduces computational costs and how different budget terms contribute to TKE in a boundary-coupled LES simulation.

Keywords: Convective Boundary Layer, Large Eddy Simulation, Nesting, Turbulence generation, Turbulence Kinetic Energy Budget

Key Points

1. The fetch is reduced after applying momentum perturbation and the reduction is directly proportional to the amplitude of the perturbations.

2. Applying momentum perturbation up to half the boundary layer height produces an adequate amount of turbulence without additional entrainment.

3. Momentum perturbations result in TKE budget terms of higher magnitude than simulations without perturbations.

Plain Language Summary

Grid nesting is a technique in atmospheric modeling where smaller model domains with finer resolutions are embedded in larger domains with coarser resolutions, allowing us to simulate processes for which a range of resolutions is important. When nesting a micro-scale domain, which resolves atmospheric turbulence, within a mesoscale domain, where turbulence is parameterized instead, the micro-scale domain needs to generate turbulence. This can take a long distance, reducing the area within the micro-scale domain where turbulence is fully developed. Turbulence generation methods can speed up this process, leading to more efficient multi-scale simulations. Here, we take a close look at one such turbulence generation method, which applies random perturbations to the momentum field along the boundaries of the micro-scale domain. We test several different configurations of momentum perturbations and evaluate their impacts on the turbulent kinetic energy budget within the micro-scale domain. Our results can be used as guidance on how to apply momentum perturbations most efficiently in grid-nested simulations.

1 Introduction

Grid nesting for mesoscale-to-large-eddy simulation (LES) is a useful technique for a variety of atmospheric model applications, from wind energy to wildfire spread investigations (Haupt et al., 2020, 2019a,b; Mazzaro et al., 2019; Mirocha et al., 2014; Ching et al., 2014; Connolly et al., 2021; Rai et al., 2017b). In LES, realistic atmospheric turbulence emerges as a result of wind shear and buoyant forcing. However, realistic turbulence can require a long distance to develop. Turbulence generation methods can accelerate the generation of turbulence in the LES domain, effectively reducing the distance it takes for turbulent motions to develop, known as fetch. A common approach is to use a periodic domain where wind through the outflow boundary is recycled through the inflow boundary, retaining memory of the flow characteristics. However, periodic simulations are limited in their ability to represent heterogeneous surfaces or flow around obstacles. For these applications, a boundary-coupled simulation with an inflow and outflow is required (Liu et al., 2011; Talbot et al., 2012; Zhou and Chow, 2013; Mirocha et al., 2014; Muñoz-Esparza et al., 2015, 2017; Mazzaro et al., 2017, 2019; Rai et al., 2017a; Jähn et al., 2016; Connolly et al., 2021). In boundary-coupled simulations using inflow data that does not contain resolved turbulence at the time and space scales of the LES discretization (e.g. from a mesoscale simulation), the development of resolved-scale turbulence generally requires a long fetch. Therefore, a large LES domain is needed (Mazzaro et al., 2017, 2019; Mirocha et al., 2014; Muñoz-Esparza et al., 2014b,a; Zajaczkowski et al., 2011; Tabor and Baba-Ahmadi, 2010) to capture the development of turbulence at fine scales, increasing computational cost (Mirocha et al., 2010, 2014; Kumar et al., 2024; Connolly et al., 2021; Muñoz-Esparza et al., 2014b; Mazzaro et al., 2017, 2019; Giani et al., 2022). Incorporating adequate representation of turbulence within the model is also advantageous in understanding the role of fire-induced turbulence in wildfire behavior particularly in the wildland-urban interface (Kumar, 2022; dos Santos and Yaghoobian, 2023; Kumar et al., 2022). The concept of "time" is used to clarify the time that a parcel of air entering the inflow boundary experiences. One way to reduce the fetch is to run a precursor LES using periodic lateral boundary conditions with the same time and space discretization as the target LES and use the solution as inflow (Muñoz-Esparza et al., 2016; Deardorff, 1972, 1980; Smith and Skyllingstad, 2009; Sauer et al., 2016; Moeng and Wyngaard, 1984; Moeng and Sullivan, 1994). However, the precursor simulation can require significant additional computational overhead, while also requiring forcing and surface conditions amenable to periodicity.

To overcome these challenges, a class of methods exists to initialize inflow boundary conditions with turbulence. For example, synthetic turbulence methods (Le et al., 1997; Pamiès et al., 2009) use digital filtering techniques of flow to infer Reynolds Stresses (Di Mare et al., 2006; Klein et al., 2003; Xie and Castro, 2008). These techniques require some information about the turbulence, either from observations or a periodic simulation. These methods also require relatively long fetches for the generation of turbulence. Another technique is the forcing method (Spille-Kohoff and Kaltenbach, 2001; Zajaczkowski et al., 2011; Keat et al., 2004), which uses wall-normal forces to move the flow into the domain inlet and generate the necessary Reynolds shear stress. However, it also needs a *priori* information about the targeted level of turbulence. Additional simulations are needed to generate an adequate amount of turbulence from this method in order to get a value that is closer to the observation.

As a compromise to using a turbulent inflow condition, another approach is to seed the inflow characteristics with added perturbations and allow the flow to develop realistic turbulence over a reduced fetch. One such method, the cell perturbation Method (CPM) (Muñoz-Esparza et al., 2014b, 2015; Muñoz-Esparza and Kosović, 2018), is a turbulence generation technique that employs random perturbations to potential temperature to induce small-scale motions near nested domain inflow boundaries. Mazzaro et al. (2019) modified the CPM approach by applying force perturbations to the momentum in the horizontal and vertical directions rather than perturbing the potential temperature fields. Mirocha et al. (2014) applied tendencies with sinusoidal amplitudes to temperature and velocity fields near inflow boundaries. This perturbation method produced promising results with the target turbulence level by triggering turbulent motions near the nested domain inflow boundaries. Muñoz-Esparza et al. (2014b, 2015), and Muñoz-Esparza and Kosović (2018) advanced this method by adding random forces instead of using sinusoidal perturbations, and also introduced perturbation cells. Perturbation cells are a span of contiguous model grid points located adjacent to the LES inflow boundaries that are perturbed with the same random value. A configuration of three cells consisting of eight grid points per cell in each of the horizontal directions is found to be optimal (Muñoz-Esparza et al., 2014b). In addition, Muñoz-Esparza and Kosović (2018) optimized the CPM for different stability conditions. Thermal perturbations are chosen to encourage the most rapid formation of realistic correlations associated with buoyancy forces generated by the patches of resolved temperature variability. Although this optimization reduces the fetch size considerably relative to simulations using no perturbations, a nontrivial fetch still remains.

To further reduce the fetch required for turbulence generation, Mazzaro et al. (2019) applied

tendencies directly to the momentum components, rather than potential temperature. This study showed that simulation perturbations that were applied to the vertical momentum term produced the shortest fetches overall, thereby further reducing fetch requirements and associated computational costs. However, the consequence of introducing momentum perturbations at the domain boundary on the fate and transport of turbulence in the domain is not yet well understood (Mazzaro et al., 2019). Quantifying the TKE budget in the Weather Research and Forecasting (WRF) LES domain can shed light on this question. In this study, we examine how momentum perturbations shift the balance between the terms of the TKE budget in the convective boundary layer (CBL). We apply random (stochastically selected from within an amplitude range of 1,000 kgs^{-4} to 10,000 kgs^{-4}) forces in both vertical and horizontal directions (Kumar et al., 2021) and vary the vertical extent of the perturbations from 307 m (halfway between the surface and boundary layer and 1,608 m (top of the domain). TKE budget terms, including buoyant production, shear production, turbulent transport, and pressure correlation are then compared between simulations including these different perturbation configurations, periodic simulations, and simulations not including perturbations.

The goals of this study are as follows: (1) to explore the impact of a simple and computationally efficient Stochastic Cell Perturbation method (SCPM) to accelerate the generation of turbulence; (2) to understand how momentum perturbations shift the balance between the terms of the TKE budget; (3) to evaluate the role of momentum perturbation amplitudes on the TKE budget; and (4) to examine the effect of height in a convective boundary layer at which momentum perturbations are applied. We use the WRF LES model to simulate the convective boundary layer. Our results will advance the understanding of optimal strategies for performing coupled mesoscale-microscale simulations of atmospheric boundary layer processes.

This study is organized into three main sections. The methods and experimental set-up that are used to perform the SCPM using momentum perturbations (SCPM-M) are presented in section 2. Section 3 describes the results and discussion of our analysis. Conclusions are presented in section 4.

2 Methods

2.1 Model Configuration

In this study, we examine the impacts of applying SCPM-M in a convective (unstable) atmospheric boundary layer on the TKE budget. We use the WRF model version 4.1.3 (Skamarock et al., 2019) to conduct idealized LES simulations of a convective boundary layer based on measurements at the Scaled Wind Farm Technology (SWiFT) facility. The SWiFT site is located in west Texas's southern Great Plains and features nearly uniform terrain elevation covered with grass and small bushes. The site contains a 200 m meteorological tower that provides fast-response velocity and temperature data at 10 heights between 0.9 and 200 m from which mean and turbulence quantities could be computed.

To conduct our analysis of the SCPM-M method, we utilized an idealized nested LES setup with forcing that approximated the observed flow conditions occurring during a two-hour period during the afternoon of November 8^{th}, 2013, 18 Z - 20 Z. We used a two-domain nested configuration for which periodic lateral boundary conditions were applied on the outer domain, and the inner domain received lateral boundary data from the bounding domain solution. The goal of the setup was to closely approximate the observed mean wind speed and atmospheric stability observed during the case study period on the outer domain. We could then examine the representation of turbulence on the inner domain and also assess the efficacy of the perturbations to accelerate the formation and fidelity of the turbulence, relative to observed values.

Since the terrain was negligible, we approximated the surface as flat, with a uniform roughness length of 0.03 m. A very close agreement between the simulated and observed wind speeds across the depth of the tower was then produced by using a constant geostrophic forcing of (u_g,v_g) = (15.331, -9.431) $ms^{-}1$, and a surface sensible heat flux of 175 W/m^2, which approximated the mean observed values from the lowest sensor height on the tower (0.9 m). These values ensured that the simulated wind direction aligned with the x-direction, allowing for the use of a nested domain elongated in the mean flow direction to facilitate the examination of the developing turbulence.

Simulations were initiated using a constant potential temperature between the surface and 250 m, with a capping inversion of 288 K/m applied up to the model top of approximately 1600 m. The simulations were run for 6 hours with the first four used for spin-up, and the latter two used for examination. The WRF domains used horizontal grid resolutions of 240 m and 12 m where the inner LES domain is one-way nested within an idealized mesoscale domain. Here, the

effective WRF grid resolution (1440 m = 6x240 m) is larger than the CBL height (600 m) and therefore the inflow conditions would not contain any resolved turbulence. The mesoscale domain (d01) has a horizontal extent of 115 km by 115 km, with 480 grid cells in both X and Y directions, while the LES domain (d02) has 961 grid cells in X direction and 481 grids in Y for a domain size of 11.5 km by 5.7 km. We use 88 vertical eta levels with the top level at 1,608 m (ztop). The minimum and maximum vertical grid spacing are 2.0032 m and 1606.5122 m respectively. An input sounding is used from the SWiFT facility with a capping inversion at approximately 600 m. The time step for integration is 0.5 seconds for the mesoscale domain and the outputs for the LES domain are stored every minute. We use a parent time step ratio of 50 and a resulting LES time step of 0.01 seconds. The general information on the model configuration is summarized in Table 2. Overall we perform nine WRF-LES simulations. The perturbation amplitudes chosen here are based on the work of Mazzaro et al. (2019), from which we selected a combination of all perturbation amplitudes, including the maximum amplitude, where each of these amplitudes is chosen at random from a uniform distribution (Mazzaro et al., 2019) that is defined by the largest perturbation value (Fxy = 5,000 kgs^{-4} & Fz = 10,000 kgs^{-4}). The conversion of force perturbation amplitude into equivalent acceleration is nonlinear because the WRF transport equations are dependent on the mass in the system (Mazzaro et al., 2019). The acceleration that results from an individual force disturbance is inversely proportional to the pressure that the atmospheric column is exerting above the affected region. Instead of simply changing the individual velocity components, we take a novel technique (SCPM-M) and change the scalar tendency of the components. The model's equations of motion are able to calculate variations in velocity because of the fluctuations we introduce in such a manner (Mazzaro et al., 2019). Seven WRF-LES simulations are performed using various permutations of perturbation height and magnitude. In addition, we also perform one simulation with no inflow perturbations (referred to as No-SCPM) and another simulation with periodic boundary conditions (referred to as periodic) for context. By using periodic boundary conditions, it is implicitly assumed that both the atmospheric fields and the underlying land usage are encountered periodically during the simulation (Mirocha et al., 2014; Zhong et al., 2021). These simulations are summarized in Table 1 and described in more detail in section 2.2.

We use the YSU (Hong et al., 2006) PBL scheme for the mesoscale domain. We do not use cloud microphysics, land surface, cumulus physics, or radiation physics in this study. We use the nonlinear backscatter and anisotropy (NBA) scheme (Kosović, 1997; Mirocha et al., 2010) to model subgrid-scale (SGS) mixing in the LES and mesoscale domain respectively. In the

LES sub-domain, the Monin-Obukhov similarity theory is used to parameterize the surface layer (surface layer option 1 (Jiménez et al., 2012; Monin and Obukhov, 1954)).

Label	**Amplitude** F_{xy} (kgs^{-4})	**Amplitude** F_z (kgs^{-4})	**Ktop** (value)	**Height** (meters)
No-SCPM	–	–	–	–
Periodic	–	–	–	–
Ktop34L	1,000	1,500	34	307
Ktop54L	1,000	1,500	54	609
Ktop88L	1,000	1,500	88	1607
Ktop88M	2,000	4,000	88	1607
Ktop34H	5,000	10,000	34	307
Ktop54H	5,000	10,000	54	609
Ktop88H	5,000	10,000	88	1607

Table 1: The table shows a list of simulations performed in this study using different Ktop values as well as the maximum amplitude of perturbations in both horizontal and vertical directions. It also shows the periodic and No-SCPM simulations used to compare the results of the SCPM-M cases.

2.2 Experimental set-up

2.2.1 SCPM Simulations

In this study, we apply momentum perturbations to 8 x 8 x 1 grid point cells from the surface up to the 34^{th}, 54^{th}, and 88^{th} pressure level along the inflow boundary of the LES domain (denoted as Ktop34, Ktop54, and Ktop88 respectively). The vertical extent of these perturbations is 307 m, 609 m, and 1,607 m, respectively. These extents correspond to heights halfway between the surface and the capping boundary layer, the height of the capping boundary layer, and the top of the domain. We also vary the perturbation amplitude. Simulations with low amplitude perturbations ($F_{xy} = 1000$ kgs^{-4}; $F_z = 1500$ kgs^{-4}) are denoted as Ktop34L, Ktop54L, and Ktop88L), and simulations with high amplitude perturbations ($F_{xy} = 5000$ kgs^{-4}; $F_z = 10000$

kgs^{-4}) as Ktop34H, Ktop54H, and Ktop88H (Table 1).

In addition, we would like to investigate whether forces lower than the higher amplitude perturbations are able to reduce the fetch in TKE generation. Therefore, we apply a combination of forces that have forcing amplitude between the higher and lower amplitude perturbations. We refer to these forces as medium amplitude perturbations. For medium amplitude perturbations (F_{xy} = 2000 kgs^{-4}; F_z = 3000 kgs^{-4}), we only perform a simulation for the Ktop88 case (denoted by Ktop88M in Table 1) for the following reason. This case involves the application of forces above the CBL height. This, in turn, gives us the opportunity to examine the impact of these forces throughout the entire inner domain, i.e., both above and below the CBL height. In contrast, applying medium amplitude perturbations at other heights (as in the case of Ktop34 and Ktop54) is devoid of this opportunity.

2.2.2 No-SCPM and Periodic Simulations

In addition to the SCPM simulations described above, we also perform a simulation where no perturbations are applied, the No-SCPM simulation. The domain configuration and simulation time for this simulation are the same as for the SCPM-M simulations.

We also compare SCPM simulations against a simulation where turbulence is developed through the use of periodic boundary conditions, i.e. output conditions at the outflow become input conditions at the inflow. We do not use nested domains for the periodic simulation. Rather, a single LES domain with 600 grid cells in X direction and 600 grids in Y is used. The domain size is 7.2 km by 7.2 km. We also use 88 vertical eta levels with the top level at 1,608 m (ztop). The input sounding remains the same as in SCPM-M simulations. The time step for integration is 0.05 seconds and the outputs for the LES domain are stored every minute. Both periodic and No-SCPM simulations are summarized in Table ref T1 SCPM M.

2.3 Analysis Methods

In order to calculate mean and turbulent statistics, we use standard turbulence decomposition, where $u' = U - \overline{U}$, $v' = V - \overline{V}$, $w' = W - \overline{W}$, and $\theta' = \theta - \overline{\theta}$ where $\overline{\theta}$. Here U, V, and W are the instantaneous velocity components, θ is the potential temperature, over-bars denote time averaging, and primes denote fluctuations from the mean. We choose time averaging to evaluate the temporal behavior and variations of mean fields to calculate perturbations in these fields in our study. The purpose is to capture the average behavior of the fields over a certain

WRF Parameters	Values
WRF version	V4.1.3
Duration of simulation	6 hours
Spin-up time	4 hours
Duration of SCPM-M	2 hours
Horizontal resolution	240 m (parent domain), 12 m (LES domain)
Vertical resolution	88 vertical eta levels
Grid spacing	480x480 (parent domain), 961x481 (LES domain)
Grid spacing (periodic)	600x600
Time step	0.5 s (parent domain), 0.01 s (LES domain)
Parent time step ratio	50

Table 2: The table shows the WRF model configuration and the summary of general information on the domain design used in this study.

time period by using temporal averaging and varying perturbations of the fields, which could potentially show interesting patterns and trends. The wind speed is calculated as $\sqrt{\overline{U}^2 + \overline{V}^2}$ with an averaging time of the last 30 minutes of simulation i.e., from 19:30 Z to 20 Z UTC (1:30 p.m. to 2 p.m. Central time). The heat flux is given by $\overline{w'\theta'}$ and momentum flux is given by $\overline{w'u'}$.

The $\overline{e}$ is the TKE, defined as:

$$\overline{e} = 0.5(\overline{u'u'} + \overline{v'v'} + \overline{w'w'}) \tag{1}$$

The turbulent kinetic energy (TKE) budget equation is given by Stull (1988):

$$\frac{\partial \overline{e}}{\partial t} + \bar{U}_j \frac{\partial \overline{e}}{\partial x_j} = \delta_{i3} \frac{g}{\overline{\theta_v}} \overline{u_i' \theta_v'} - \overline{u_i' u_j'} \frac{\partial \bar{U}_i}{\partial x_j} - \frac{\partial \overline{u_j' e}}{\partial x_j} - \frac{1}{\overline{\rho}} \frac{\partial \overline{u_i' p'}}{\partial x_i} - \epsilon \tag{2}$$

The first and second terms on the left-hand side (LHS) of equation 2 represent local storage or the tendency of TKE and the advection of TKE by mean wind, respectively. The terms on the right-hand side (RHS) of equation 2 in order from left to right represent the buoyant production or consumption term, a mechanical or shear production term, the turbulent transport of TKE, a pressure correlation term, and the viscous dissipation of TKE, respectively (Stull, 1988).

The TKE budget equation after assuming horizontal homogeneity, neglecting subsidence, and choosing a coordinate system that is in the direction of mean wind, is simplified as:

$$\frac{\partial \overline{e}}{\partial t} = +\frac{g}{\overline{\theta_v}}\overline{w'\theta'_v} - \overline{u'w'}\frac{\partial \bar{U}}{\partial z} - \frac{\partial \overline{w'e}}{\partial z} - \frac{1}{\overline{\rho}}\frac{\partial \overline{w'p'}}{\partial z} - \epsilon \tag{3}$$

Using these concepts and equations, we compute TKE, heat, and momentum fluxes, as well as TKE budget terms associated with buoyancy, shear, transport, and pressure correlation for all simulations outlined in Table 1. In the next section, we present and discuss the results of this analysis.

3 Results and Discussion

3.1 Turbulent kinetic energy (TKE)

3.1.1 Spatial variation of TKE

TKE is a measure of the intensity of turbulence. We calculate TKE for all simulations (Table 1) and compare its variation over height (z) and streamwise distance (x) (Figure 1). The distance from the inflow boundary at which turbulent fluctuations start to develop is called fetch (Mazzaro et al., 2017, 2019). We observe that for simulations without momentum perturbation (No-SCPM), turbulence begins to develop 5,000 m into the domain, with a significant fetch, and a realistic representation of fully developed turbulent structures only appears in the last 25% of the domain. After applying SCPM-M, the fetch is reduced significantly for all perturbed cases.

For high amplitude perturbations (Figure 1b-d), the fetch is diminished, but the maximum of TKE is present along the inflow boundary and near the boundary layer top. For Ktop54H and Ktop88H, positive values of TKE extend above the boundary layer, an artifact related to the high perturbation height and amplitude (Figure 1c) and Figure 1d). Furthermore, for Ktop34H, the TKE maximum is present near the bottom of the domain, near the surface and most importantly, the fetch has reduced significantly (Figure 1b).

In the case of lower and medium amplitude perturbations (Figure 1(e-h)), the TKE maxima near the boundary layer are not present. We also observe that the rate at which the TKE increases with the downwind x direction is similar for the medium and lower amplitude perturbations but not the same as the No-SCPM case (Figure 1a).

These spatial patterns highlight that the vertical and horizontal extent of inflow perturbations can influence the underlying turbulence evolution. Moreover, SCPM-M produces a vertical profile of TKE that spans the boundary layer more rapidly than without the perturbations. In addition, tuning the amplitude of the perturbation helps minimize the fetch to fully develop the TKE. Here, the term "fully developed" we do not mean that TKE has reached the exact same value, but rather the same order of magnitude. However, if the height of perturbations approaches or exceeds the boundary layer, this leads to artifacts in the flow field above the boundary layer height.

3.1.2 Fetch

In boundary-coupled simulations using inflow data that does not contain resolved turbulence at the time and space scales of the LES discretization (e.g. from a mesoscale simulation), the development of resolved-scale turbulence generally requires a long fetch. We compare the variation of Y-averaged TKE over height and longitude in the y and x axes respectively (at two heights, 10 m, and 53 m, Figure 2) from the perturbed cases and the periodic simulation to investigate the extent of the fetch. The distance from the inflow boundary at which the TKE from the SCPM-M simulations becomes comparable to the TKE obtained from the periodic simulation can be used as a rough estimator for the fetch. The fetch required to fully develop turbulence is referred to as 'required fetch' hereafter.

We observe that the required fetch is the longest for No-SCPM simulation (Figure 2a). At 10 m height, the required fetch for the No-SCPM case is around 9,000 m, and at 53 m the fetch is around 7,200 m (Figures 2a-d). Before the fetch is fully established, the TKE increases to an unrealistically high level as indicated by the large departure from the periodic case.

However, after applying SCPM-M, the required fetch is reduced significantly. At both 10 m and 53 m, the TKE is fully developed around 2,000 m for all perturbed cases as shown in Figure 2. Quantitatively, we find that the TKE reaches 80% of its steady-state magnitude at 2000 m from the inlet boundary in the case of SCPM-M simulations when compared to the periodic simulation (Figure 2). On the other hand, the No-SCPM scenario takes 5000 m to achieve the same level of TKE. At the last quarter of the domain, starting at $x = 9,600$ m, the TKE for the perturbed cases is quite close to the periodic case. Therefore, we will use the last three-quarters of the domain (x from 2,880 m to 11,520 m) to average over turbulence statistics subsequently reported in this study. The TKE profiles averaged over the last quarter of the domain (x from 86,400 m to 11,520 m) will be reported only for reference in section 3.1.3. Furthermore, the TKE evolves over

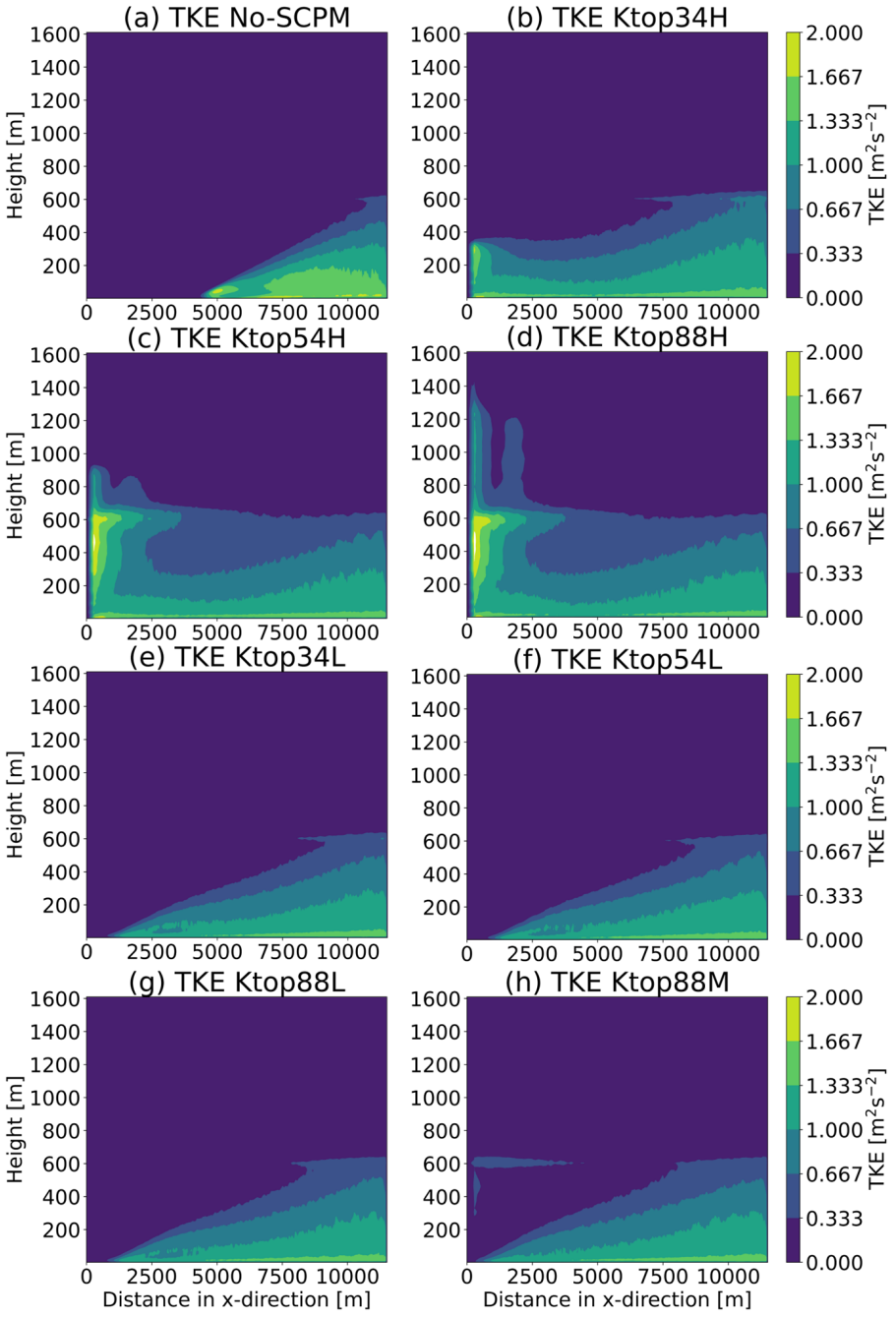

Figure 1: Y-averaged TKE (m^2/s^2), computed over the entire inner domain, compared between simulations with and without momentum perturbation with different perturbation amplitudes and vertical extents with panels (a) No-SCPM, (b) Ktop34H, (c) Ktop54H, (d) Ktop88H, (e) Ktop34L, (f) Ktop54L, (g) Ktop88L, and (h) Ktop88M as shown in Table 1.

time and space after applying SCPM-M. For instance, we can see this spatial evolution when we compare the area-averaged TKE over the last quarter of the domain to the area average over the last three-quarters of the domain. The former is much closer to the periodic value than the latter. For more information on the effects of the spatial averaging domain on fluxes and TKE budget terms, please see the supplementary material (Subsection S4.1).

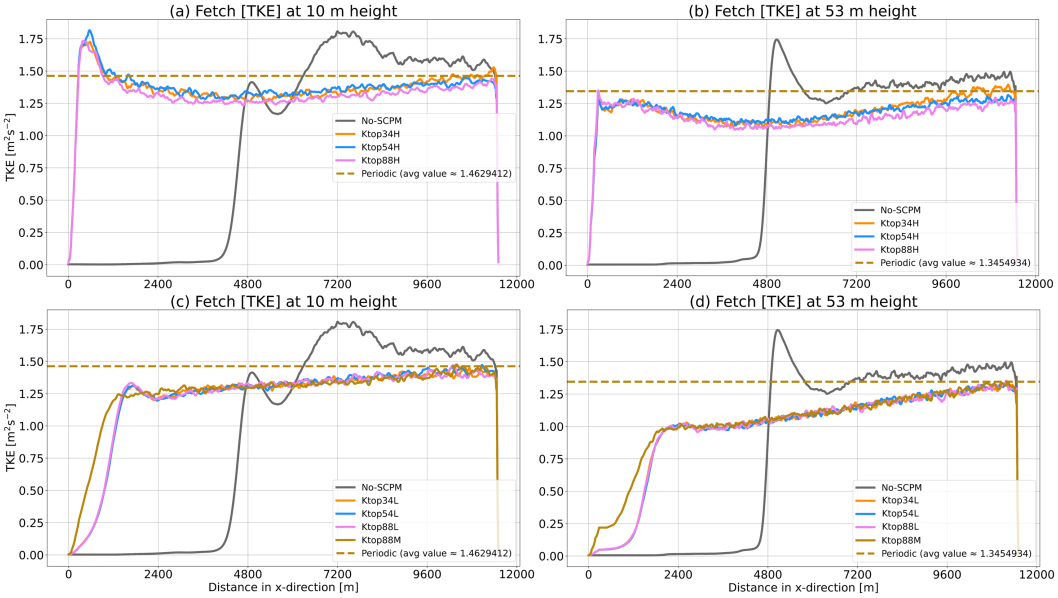

Figure 2: Fetch of Y-averaged TKE (m^2/s^2), computed after applying momentum perturbation with higher, medium, and lower amplitudes as shown in (Table 1) and show fetch at (a) 10 m height for periodic, No-SCPM, and higher amplitude SCPM-M, (b) 53 m height for periodic, No-SCPM, and higher amplitude SCPM-M, (c) 10 m height for periodic, No-SCPM, and lower and medium amplitude SCPM-M, (d) 53 m height for periodic, No-SCPM, and lower and medium amplitude SCPM-M. These plots are generated for TKE that are Y-averaged over the entire inner domain.

3.1.3 TKE profiles

Based on the discussion in the previous section 3.1.2, we compare the TKE profiles that are averaged over two different areas: three-quarters of the domain (overall y and x from 2,880 m to 11,520 m) farthest away from the inflow (Figures 3 (a-b)), and last quarter of the domain (overall y and x from 86,400 m to 11,520 m) farthest from the inflow (Figures 3 (c-d)). We observe that applying SCPM-M produces TKE closer to the periodic case regardless of the extent of its application (Figures 3(a-d)).

As it is observed in Figure 3, the TKE is highest near the surface and decreases with height in

all SCPM-M simulations and as well as in the case of No-SCPM. Up to 200 m, the TKE is similar for all the perturbed cases as well as the periodic case, while the TKE for the No-SCPM case is lower, when the TKE is area-averaged over the last three-quarters of the domain (Figures 3a-b). However, between 300 m and up to the CBL height, SCPM-M cases with higher amplitudes (Ktop34H, Ktop54H, and Ktop88H) are closer to the periodic case; while No-SCPM shows the largest deviation from the periodic case (Figures 3a-b). When the last quarter area-averaged profiles are compared (Figures 3c-d), we find that the TKE is highest for No-SCPM case below 300 m and it decreases sharply above 300 m, deviating the most from the periodic case. However, the SCPM-M cases are closer to the periodic case for all heights. In addition, we also observe that the medium and lower amplitude SCPM-M cases are almost equal in magnitude throughout the domain (Figure 3d). From the high amplitude SCPM-M cases, the TKE for the Ktop34H is closest to the periodic case above 300 m (Figure 3c). It is important to note that the effect of momentum perturbation is not only to enhance TKE but rather to adjust TKE closer to the appropriate levels at all heights within the CBL. Therefore, even though SCPM-M is shown to correct less than half the bias while TKE is evolving, measured as the difference in TKE values between the periodic simulation and the No-SCPM simulation, for a significant portion of the CBL, it performs better than No-SCPM for a significant portion of the CBL.

3.2 Mean and instantaneous flow features

3.2.1 Instantaneous flow features

Figure 4 shows the instantaneous U component of velocity at two-thirds and half of the CBL height (211 m and 391 m, respectively) for simulations without SCPM and the SCPM applied to three different vertical extents. These velocities are shown at the last instant of the simulation period i.e., at 20 Z (UTC) for the nested LES domain. As observed in Figures 1,2, and 3, and in previous studies, such as Mazzaro et al. (2017, 2019), a large fetch is required for the No-SCPM simulation. The fetch is reduced significantly whenever perturbations are applied, regardless of the extent and amplitude of the applied momentum perturbation.

3.2.2 Mean wind speed profiles

We find that the time and area-averaged (over the last 30 minutes of simulation for the last three-quarters of the domain) vertical profiles of the wind speed for the different simulation cases have a logarithmic profile near the surface layer up to the height of 200 m (Figure 5a).

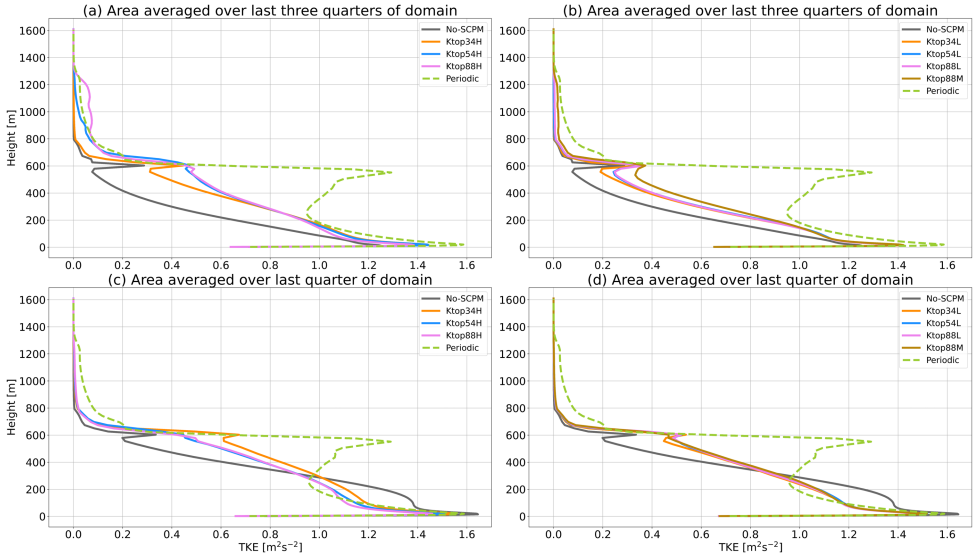

Figure 3: Area-averaged TKE (m^2/s^2) profiles, computed for the inner domain after applying momentum perturbation with higher amplitude (Table 1) in the right panels and lower & medium amplitudes (Table 1) in the left panels, respectively. Profiles (a) and (b) show TKE values that are area-averaged over the last three-quarters of the domain, i.e., overall y and x from 2,880 m to 11,520 m for (a) Periodic, No-SCPM, and high amplitude SCPM-M (Ktop34H, Ktop54H, and Ktop88H); (b) Periodic, No-SCPM, and low and medium amplitude SCPM-M (Ktop34L, Ktop54L, Ktop88L, and Ktop88M). While, panels (c) Periodic, No-SCPM, and high amplitude SCPM-M (Ktop34H, Ktop54H, and Ktop88H), and (d) Periodic, No-SCPM, and low and medium amplitude SCPM-M (Ktop34L, Ktop54L, Ktop88L, and Ktop88M) are the TKE profiles that are area-averaged over only the last quarter of the domain, i.e., overall y and x from 86,400 m to 11,520 m.

In this study, we are interested in the lower atmospheric boundary layer (200 m), focusing on applications such as wind energy. We used the term "surface layer" as 10-20% of the boundary layer height. Under convective conditions, the profiles of mean velocity would not be perfectly logarithmic, but one can use Monin-Obukhov Similarity Theory (MOST) to obtain stability correction functions. However, in this case, since very mildly unstable conditions are used, we did not focus on stability corrections. The extent and amplitude of inflow perturbations have a small effect on the wind speed profiles. Between 100 m to 500 m, the wind speed for the No-SCPM case is higher as compared to the other perturbed cases. Between 100 m to 500 m, the lowest wind speed is observed for the periodic simulation (dashed line) followed by the Ktop88H case (purple line) Figure 5(a-b), compared to the other cases. Wind speed profiles for the lower and medium SCPM-M cases are similar to each other but lower than the No-SCPM case up to about 500 m. We evaluated the model's capacity to accurately represent the atmospheric conditions

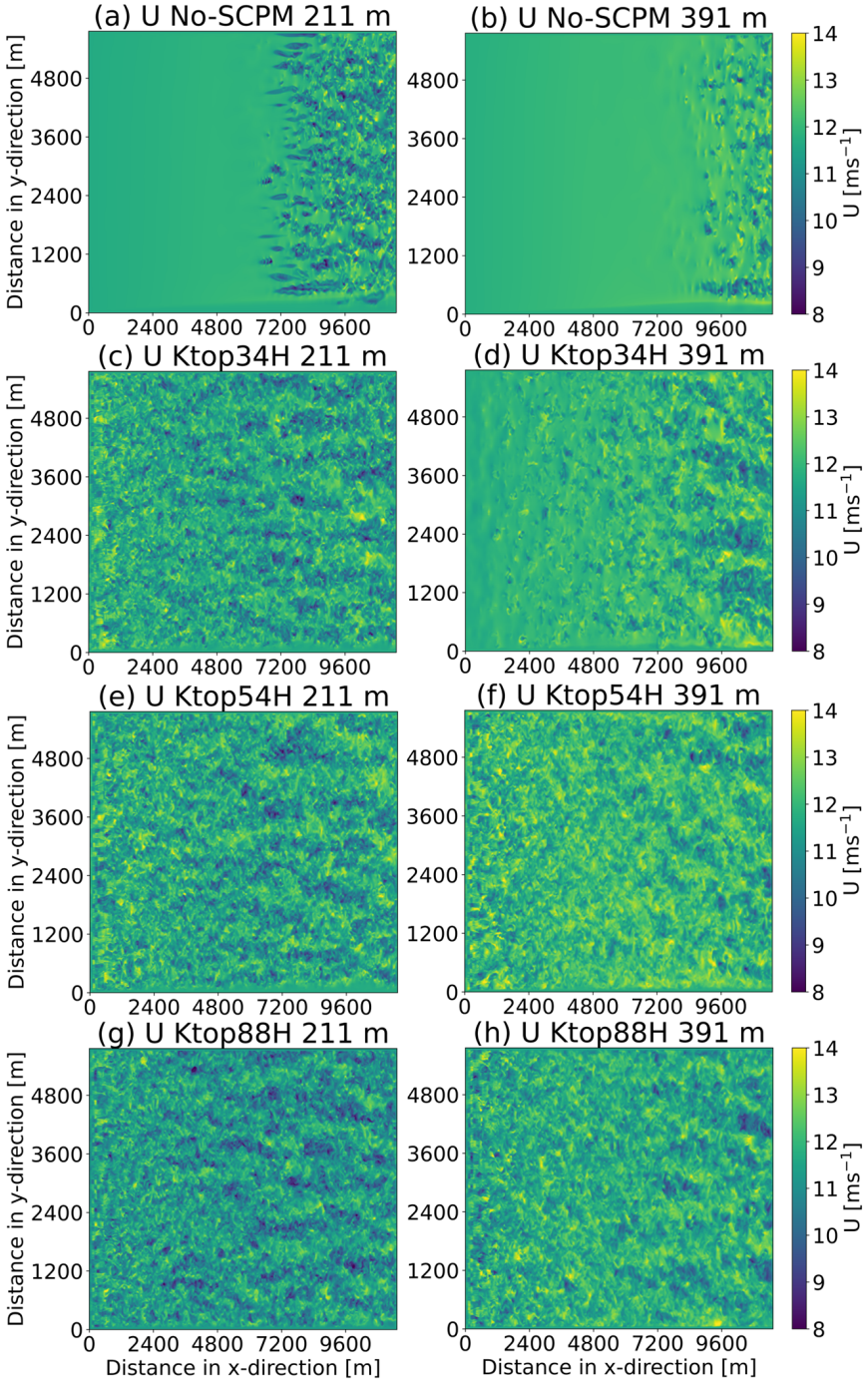

Figure 4: Instantaneous U component of velocities (ms^{-1}), computed at two different heights that are at half (level=27, z=211 m) and at two-thirds (level=37, z=391 m) of the boundary layer height for (a-b) No-SCPM, (c-d) Ktop54H (e-f) Ktop54H (g-h) Ktop88H. The color bar corresponds to the magnitude of velocity for panels (a) to (h).

and enhance our confidence in the results by comparing the model results with the tower data that is currently available in the form of observations from the SWiFT site. We compare the observational wind speed (Figure 7a) and potential temperature (Figure 7b) profiles with model results at three different instances i.e., 18 Z, 19 Z, and 20 Z 7. Figure 7(a-b) shows reasonable agreement between the sounding and model wind speed and very good agreement for potential temperature respectively, for the lower 200 m of the atmosphere for all three times.

3.2.3 Velocity variance statistics

In order to examine the contributions of the velocity variance components (σ_u^2, σ_v^2, σ_w^2) to the TKE, we area-average them over the last three-quarters of the domain and compute in Figure 6. The notations with primes and overbars for variance are indicated with sigmas and subscripts. Similar to the TKE profiles in Figure 3, all three velocity variances are higher for the SCPM-M cases compared to the No-SCPM case. The σ_w^2 is higher for the Ktop34H case around 200 m. Just below the CBL height of 600 m, the σ_u^2 and σ_v^2 are higher for Ktop88H compared to the other cases.

3.3 Fluxes of sensible heat and momentum

Similar to the other turbulence statistics, the fluxes of sensible heat ($\overline{w'\theta'}$) and momentum ($\overline{u'w'}$) are averaged over the last three-quarters of the domain and plotted in Figure 8. We observe that below 200 m, the fluxes of sensible heat and momentum are higher for the No-SCPM case as compared to the SCPM-M cases (Figure 8). This could be attributed to unrealistically high levels of TKE in the No-SCPM case in the last two-quarters of the domain, as observed in Figure 2. Above 200 m, the sensible heat flux for the SCPM-M cases is similar to the No-SCPM case (Figure 8(a-b)). However, the momentum fluxes are higher for the SCPM-M cases than the No-SCPM (Figure 8c-d) case above 200 m.

Among the SCPM-M cases, the Ktop34H has a higher magnitude of sensible heat flux than the other cases (Figure 8a). Here, we use the SI prefix 'k' for 'kilo' for the heat flux unit as it has a high magnitude during a convective case. The lower and medium amplitude SCPM-M cases are similar in the sensible heat flux throughout the domain (Figure 8b). For the momentum flux, all high amplitude SCPM-M cases (Figure 8c) and all the low and medium amplitude cases (Figure 8d) are similar to each other.

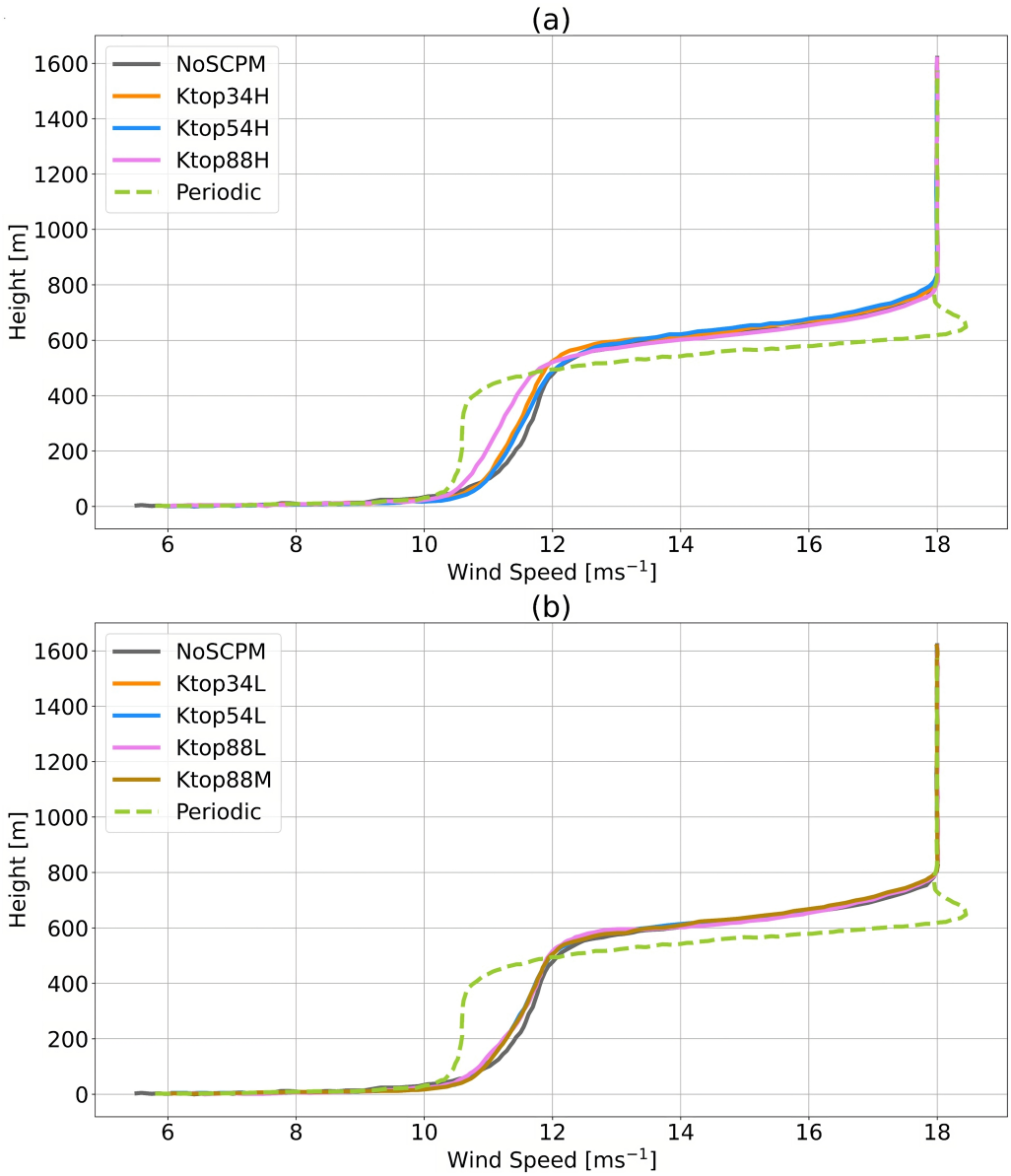

Figure 5: Wind speed (ms^{-1}) area-averaged over three-quarters of the domain (all y and x from 2,880 m to 11,520 m) for all the cases as shown in Table 1 for (a) higher, (b) lower and medium amplitude SCPM-M as well as No-SCPM and periodic simulation. The wind speeds are generated from the last 30 minutes of the simulation time period i.e., from 19 Z (UTC) to 20 Z (UTC) and for the top of the entire simulation inner domain up to 1608 m.

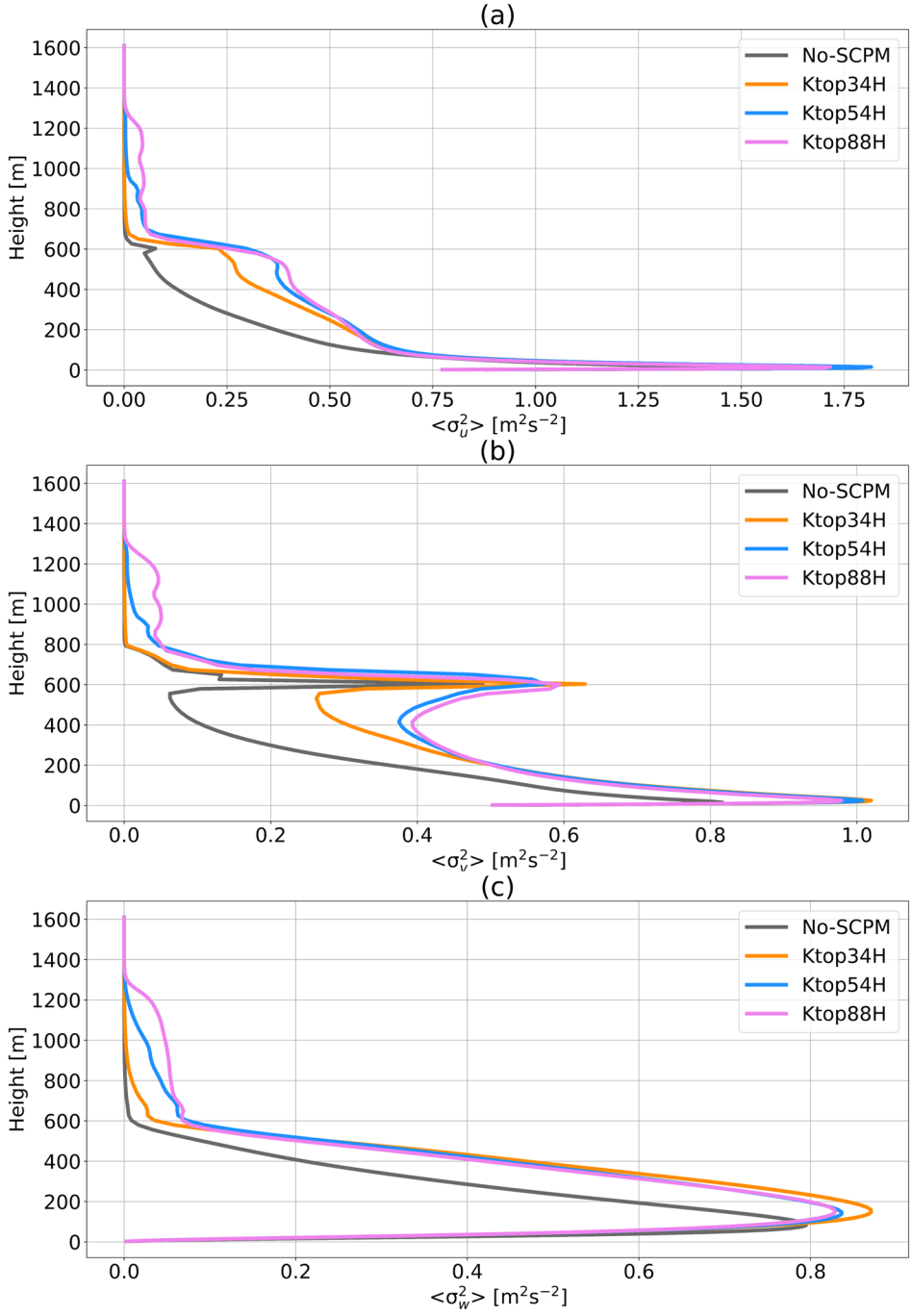

Figure 6: Area-averaged (a) $< \sigma_u^2 >$, (b) $< \sigma_v^2 >$, and (c) $< \sigma_w^2 >$ over three quarters of the domain (all y and x from 2,880 m to 11,520 m) for No-SCPM, Ktop34H, Ktop54H, & Ktop88H. These results are shown from the last simulation period at 20 Z and for the top of the entire simulation inner domain up to 1,608 m. The angular brackets denote area averaging.

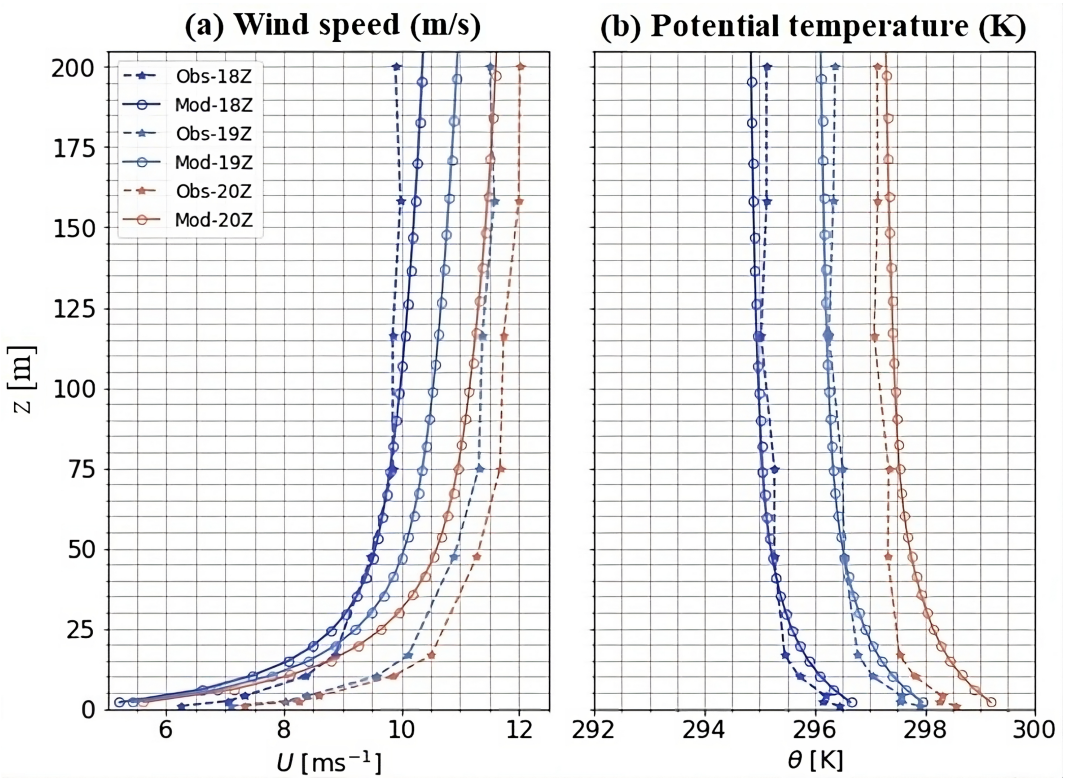

Figure 7: Profiles of domain-averaged (a) wind speed and (b) potential temperature at hours 18, 19, and 20 Z (UTC) during assessment (18-20Z) periods, versus centered 30-minute-averaged quantities observed at the SWiFT.

At the top of the inversion layer, Ktop34H has the highest entrainment flux (this is where the 'potentially' warmer air is entrained into the CBL), as indicated by the strongly negative sensible heat flux at the top of the CBL for Ktop34H. Ktop88H and Ktop54H simulations produce similar entrainment fluxes of heat from above into the CBL. This is due to turbulence being artificially excited near and above the top of the CBL.

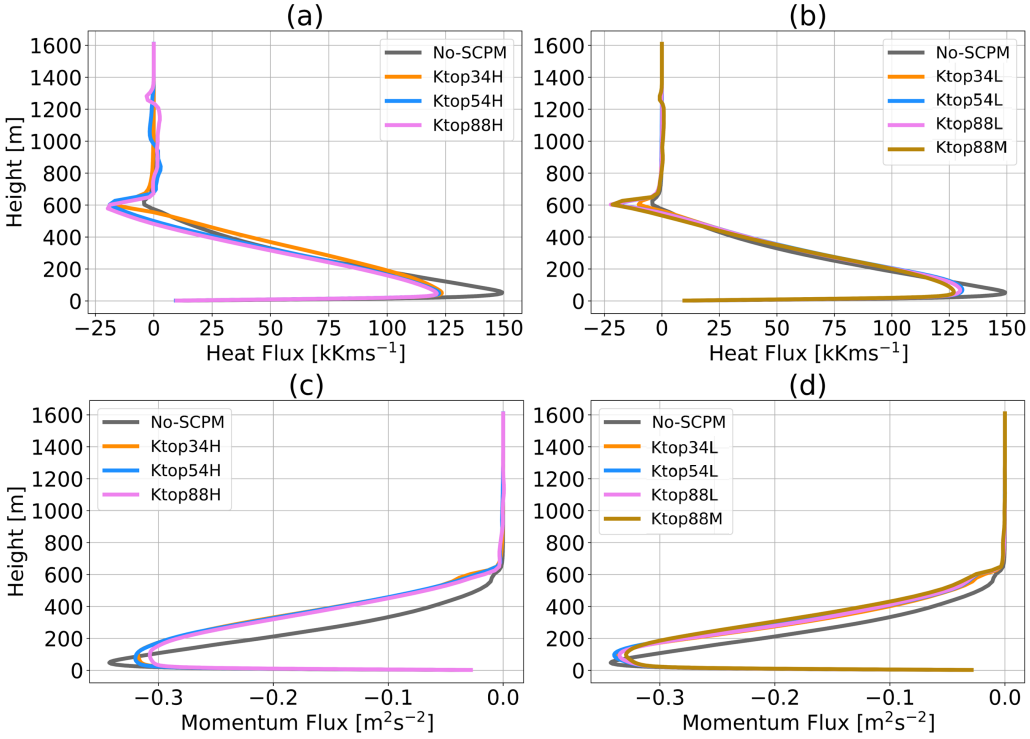

Figure 8: Heat flux ($\overline{w'\theta'}$) profiles after applying momentum perturbation (SCPM-M) with (a) higher amplitudes of forces, as shown in (Table 1), (b) lower & medium amplitudes of forces; momentum flux ($\overline{u'w'}$) with (c) higher amplitudes of forces, and (d) lower & medium amplitudes of forces. In addition, these profiles are computed in a way that the heat flux ($\overline{w'\theta'}$) and momentum flux ($\overline{u'w'}$) are area-averaged over the last three-quarters of the inner domain i.e., overall y and x from 2,880 m to 11,520 m and are shown for the top of the entire simulation inner domain up to 1608 m.

3.4 Turbulent kinetic energy budget

Since sensible heat flux and momentum flux contribute to TKE generation, the components of the budget equation for the TKE are worth investigating for the simulated cases. Therefore, individual terms of the TKE budget are discussed in this section. Figure 9 shows the y-averaged

components of the TKE budget for the No-SCPM (left column) and the Ktop34H case (right column). We focus our discussion on the Ktop34H case because (1) additional entrainment at the capping inversion level is very low compared to the other cases, and (2)the reduction in fetch is significant. The other high amplitude cases, while reducing the fetch, generate additional entrainment at the CBL height. In contrast, the low amplitude and medium amplitude cases are less efficient in the fetch reduction.

The y-averaged TKE budget terms for other SCPM-M cases are plotted in the supplementary material (Figure S14). Vertical profiles of the TKE budget terms, averaged over the three quarters farthest from the inflow of the domain are shown in Figure 10 for all SCPM-M cases as well as the No-SCPM case.

3.4.1 Buoyancy Term

The y-averaged buoyancy term $(g/\overline{\theta})\overline{w'\theta'}$ for the No-SCPM and Ktop34H cases are plotted in Figure 9a and b.

We observe that for the No-SCPM case, the buoyancy term starts developing from the center of the x axis (Figure 9a). However, the fetch for the buoyancy term is reduced significantly for the perturbed cases (Figure 9b) and Figure S14). For Ktop54H and Ktop88H, the fetch is reduced appreciably, however, additional entrainment can be observed near the CBL height (Figure S14a-b). In general, lower amplitude perturbations reduce the fetch and do not create additional entrainment. Another important point to note is that the application of momentum perturbation (SCPM-M) is sufficient to modify the buoyancy term, without requiring perturbing the temperature field, as demonstrated by Mazzaro et al. (2019). This could be explained by the fact that the force-perturbation method generates additional w' fluctuations in the turbulent field, which excites the vertical sensible heat flux $\overline{w'\theta'}$ as well.

As observed in Figure 10a-b, the vertical profile of the buoyancy term follows the same trend of the sensible heat flux profiles as shown in Figure 8a-b.

3.4.2 Shear Term

The momentum flux $\overline{u'w'}$ is negative as momentum is absorbed towards the ground, and therefore the term $-\overline{u'w'}(\partial U/\partial z)$ is positive and a source of TKE. Without applying momentum perturbation, we find that WRF-LES is unable to generate shear production (Figure 9c) from the very

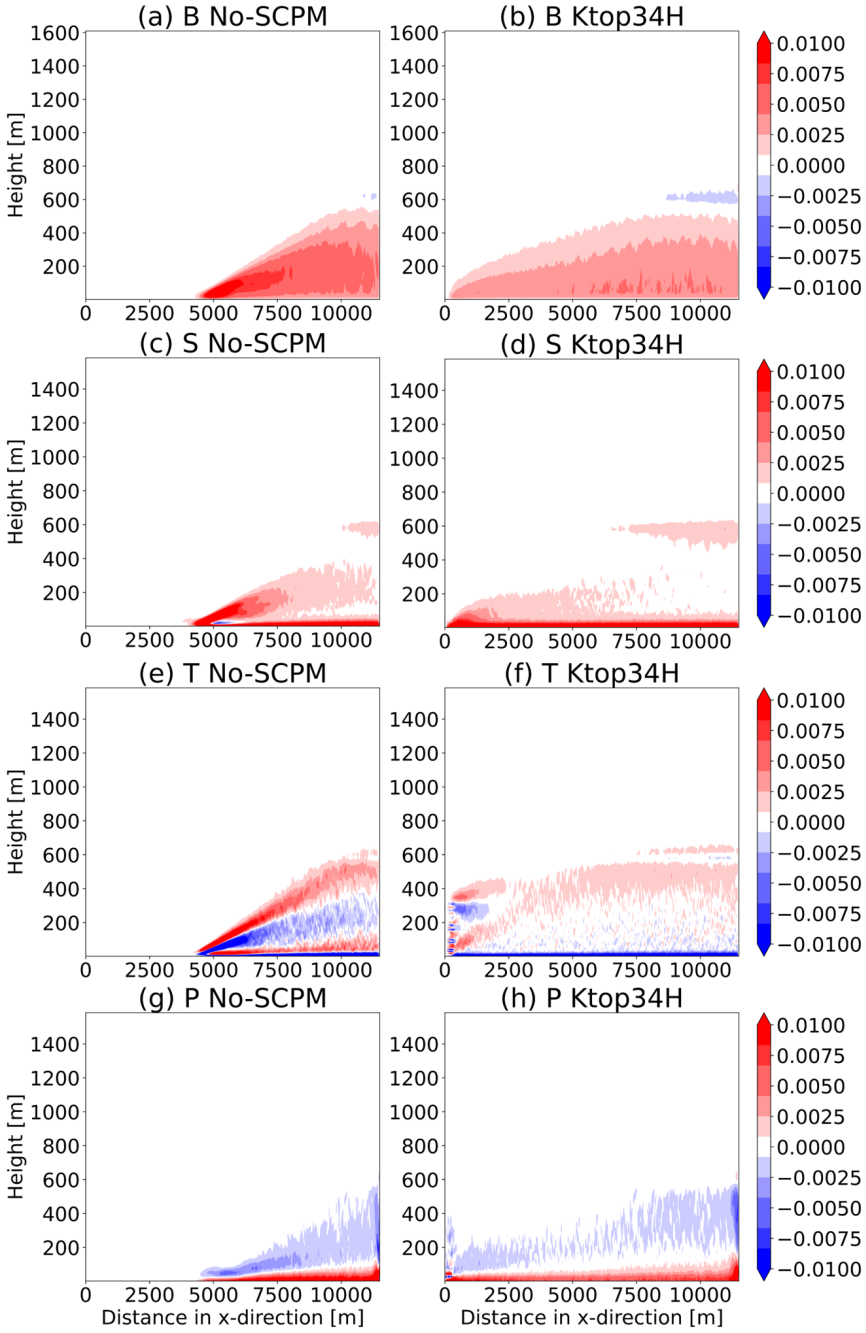

Figure 9: Y-averaged TKE budget terms after applying momentum perturbation following (Table 1), for the buoyancy term with (a) No-SCPM, (b) Ktop34H, for the shear production term with (c) No-SCPM (d) Ktop34H, for the turbulent transport with (e) No-SCPM (f) Ktop34H, and for the pressure correlation term with (g) No-SCPM, (h) Ktop34H. The color bar corresponds to the magnitude of TKE budget terms for panels (a) to (h). These plots are generated for TKE budget terms that are Y-averaged over the entire inner domain.

beginning of the lateral boundary and thus results in a long fetch before turbulence develops, as observed in the plan-view plots of velocities (Figure 4 and Figure S12). Since applying SCPM-M reduces the fetch in velocity generation, in a similar fashion, the fetch in shear production is also reduced because it is a combination of both (u and w) quantities ($-\overline{u'w'}(\partial U/\partial z)$).

We find that SCPM-M with higher amplitudes reduces the fetch in shear production significantly, as shown in Figure 9d. However, in Ktop54H and Ktop88H, strong shear production is observed at the beginning of the LES domain near the lateral boundary (Figure S15a-b). This can be attributed to the application of SCPM-M near and above the CBL, which produces superfluous turbulent motions and ultimately contributes to strong shear production above the CBL. Furthermore, we observe a small to moderate intensity of shear production near the CBL height for the SCPM-M cases due to a strong $\partial U/\partial z$ in the last quarter of the domain (Figure 9d). Other SCPM-M cases are shown in the supplementary materials. In other SCPM-M cases with lower and medium amplitudes (Figure S15c-f), the fetch is reduced to a great extent without the generation of spurious motions near the lateral boundary at the beginning of the innermost domain.

Applying momentum perturbation within the LES domain contributes to maximum shear production near the surface in all the cases, as shown in Figure 10c-d. When compared to the No-SCPM case, the largest magnitude of shear production with SCPM-M is higher below the height of 200 m. There is a small but sharp jump in the shear term near the entrainment zone, regardless of the amplitudes of SCPM-M. Shear production reaches zero just above the CBL in all the SCPM-M cases. It diminishes completely at 650 m above the surface.

3.4.3 Turbulent Transport Term

In a planar homogeneous case without subsidence, the turbulent transport term in the TKE budget integrates over the domain height to null, indicating that TKE is transferred among horizontal planes (Stull, 1988). The $\overline{w'e}$ is the major contributor to the turbulent transport term in the TKE budget equation. Here, we compare the y-averaged turbulent transport terms for different SCPM-M cases. Furthermore, the planar homogeneous assumption is on the boundary condition and land cover and it is not on the flow itself. In addition, even with the planar homogeneous flow boundary condition, the TKE needs space to develop.

Beyond $x = 4,800$ m, gain due to turbulent transport (T>0) alternates with loss due to turbulent transport (T<0), as we ascend along the $y - axis$ up to the CBL height in the No-

SCPM case (Figure 9e). After applying SCPM-M, redistribution of the TKE starts at the beginning of the domain, as shown in Figure 9f (Figure S16a-f shows all the other cases for the sake of completion). Therefore, the fetch in the generation of the turbulent transport term is reduced significantly with SCPM-M. However, the SCPM-M cases with higher amplitude produce more entrainment near the inflow boundary as compared to the lower amplitude SCPM-M cases (Figure 9f and Figure S16a-f). Among the higher amplitude SCPM-M cases, Ktop34H produces lower entrainment (Figure 9f and Figure S16a-b). The entrainment is not produced for the lower amplitude SCPM-M cases (Figure S16c-e).

We also compute the profiles of the turbulent transport terms that are area-averaged over the last three-quarters of the domain (all y and x from 2,880 m to 11,520 m) for the simulations in this section (Figure 10e-f). We find that without the SCPM-M, the turbulent transport term increases up to 25 m and then continuously decreases up to 140 m, and then increases again up to the bottom of the CBL. Finally, it ($\overline{w'e}$) sharply decreases to null at the CBL top (Figure 10e-f).

In the case of SCPM-M with higher amplitudes, the changes are more abrupt within the CBL and it approaches zero slightly above and below the CBL height (Figure 10e). Also, at higher amplitudes, their profiles are not exactly the same but are slightly different throughout the boundary layer up to the CBL top (Figure 10e). However, at the lower and medium amplitude SCPM-M cases, the turbulent transport terms are almost similar to the No-SCPM case above 200 m (Figure 10f). Similar to the higher amplitude SCPM-M cases, $\overline{w'e}$ reaches zero slightly above and below the CBL height (Figure 10f) for the lower and medium amplitude SCPM-M cases.

3.4.4 Pressure Correlation Term

The pressure correlation term plays the role to redistribute TKE within the boundary layer. Additionally, in some cases, the pressure covariance does not dissipate energy but transfers it out of the boundary layer through gravity waves (Stull, 1988). Applying SCPM-M significantly reduces the fetch in the redistribution of TKE through the pressure correlation term, and the area-averaged profiles become smoother, as shown in Figure 10g and Figure S17a-f. The redistribution of TKE starts from the beginning of the domain with higher and medium amplitude perturbations, while it starts after $x = 100\,m$ for the lower amplitude SCPM-M cases (Figure 9h and Figure S17a-f). In the case of Ktop54H and Ktop88H, we observe some spurious motions at

the beginning of the domain (at the inflow boundary), as shown in Figure S17a-b.

We observe that applying momentum perturbation results in a higher magnitude of pressure correlation terms as compared to the No-SCPM case (Figure 10g-h). The magnitudes of these terms are slightly higher in the case of SCPM-M with higher amplitudes as compared to the SCPM-M cases with lower amplitudes (Figure 10g-h). The differences among higher and lower amplitude SCPM-M cases are not significant below 100 m as there are very low magnitudes of pressure fluctuations in the surface layer (i.e., the lowest 10% of the boundary layer).

3.4.5 Temporal evolution of TKE

In this subsection, we investigate the evolution of the TKE with time to examine how long the effect of the momentum perturbation last after the perturbations are turned off. And then, if we want to maintain the sustained turbulence in the atmosphere, how frequently should we add these perturbations? We would like to clarify that it is neither about the lingering effects of perturbations nor about the application of perturbation during day and night. The SCPM-M simulations are performed for two hours, starting from 18 Z (UTC) to 20 Z (UTC). The application of external forces creates inertia, which is present for the next half an hour from the time when the momentum perturbation is stopped. As shown in Figure 11, although the magnitude of TKE that is generated due to inertia is low, it still remains finite from 20 Z to 20:30 Z in the two cases, i.e., Ktop54H and Ktop88H (11(a and c)) (Ktop34H is not shown here but similar results are expected). Comparing the results after 20:30 Z, Figure (11(a and c)) and Figure (11(b and d)), it is clear that the TKE dissipates and the effect of inertia is no longer present after 20:30 Z (UTC).

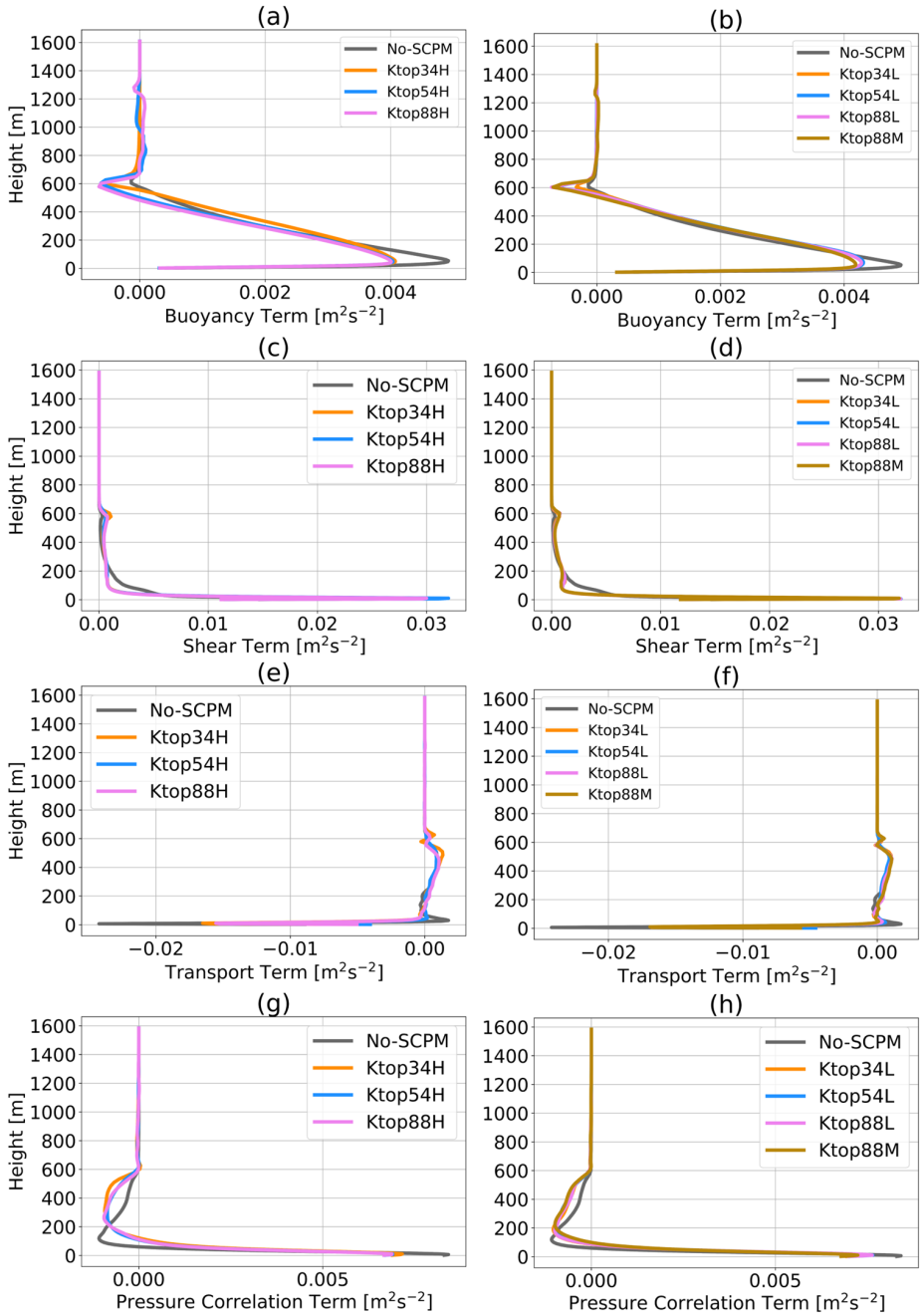

Figure 10: Area-averaged TKE budget terms over the last three-quarters of the domain, i.e., overall y and x from 2,880 m to 11,520 m after applying momentum perturbation for the buoyancy term with (a) higher amplitudes, (b) lower and medium amplitudes; for the shear production term with (c) higher amplitudes (d) lower and medium amplitudes; for the turbulent transport with (e) higher amplitudes (f) lower and medium amplitudes; and for the pressure correlation term with (g) higher amplitudes, (h) lower and medium amplitudes. These plots are shown for the top of the inner domain from simulation (up to 1,608 m).

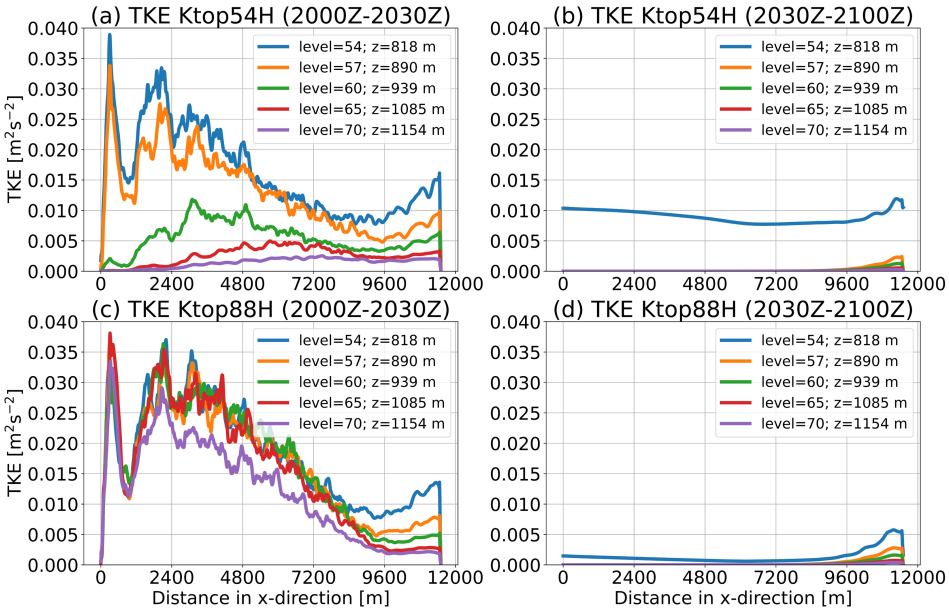

Figure 11: Y and time-averaged TKE (m^2/s^2) profiles, computed at different heights in the atmosphere during an unstable case when momentum perturbation was turned off from (a) 20 Z to 20:30 Z (UTC) for Ktop54H, (b) 20:30 Z to 21:00 Z (UTC) for Ktop54H, (c) 20 Z to 20:30 Z (UTC) for Ktop88H, and (d) 20:30 Z to 21:00 Z (UTC) for Ktop88H in the different panels of the figure. These profiles are generated for buoyancy terms that are area-averaged over the entire inner domain.

4 Conclusions

In this work, we studied the impact of momentum perturbations, employed to generate turbulence in boundary-coupled LES simulations, on the turbulent kinetic energy (TKE) budget terms in an unstable boundary layer. It is well known that LES models that are used with periodic boundary conditions are capable of representing fully developed turbulence. However, turbulence representation is challenging in models that couple mesoscale and microscale domains or when conducting LES simulations with non-periodic conditions, such as in the presence of complex topography. Additional turbulence-generation techniques are needed in these instances. Several such techniques had been developed in the past, each one with its own advantages and disadvantages. Here, we implemented the stochastic cell perturbation technique in WRF-LES simulations to study the impact of turbulence generation on the TKE budget. We used an LES domain with a horizontal resolution of 12 m, which was nested within a mesoscale domain with a horizontal resolution of 240 m. Momentum perturbations were applied in the horizontal and vertical directions at the inflow boundaries of the LES domain. We performed experiments where we varied perturbation amplitudes, as well as the heights to which the perturbations were applied with respect to the CBL height.

Applying SCPM-M accelerated turbulence generation, and significantly reduced the fetch, for all cases studied. Fetch reduction in coupled mesoscale-microscale atmospheric simulations results in lower computational costs of numerical experiments since a smaller domain would need to be resolved. While the magnitude of TKE produced was always higher for the SCPM-M cases than the No-SCPM case, we found that turbulence strength depended on the amplitude of perturbations, with higher-amplitude perturbations producing more turbulence than medium and lower-amplitude perturbations. Simulations with perturbations produced larger variances in the velocities up to the inversion layer than No-SCPM simulations. This also contributed to higher heat and momentum fluxes. We found that SCPM-M simulations provided comparable results with observations and that the model outputs are consistent with it. In summary, atmospheric stability plays a critical role in the generation and evolution of turbulence in the boundary layer. Stable atmospheric conditions suppress turbulence generation, while unstable conditions enhance it.

The perturbations also affected buoyancy production. SCPM-M simulations produced slightly more buoyancy than the No-SCPM case in the bottom and top third of the boundary layer, while buoyancy in the SCPM-M simulations was comparable to that in the No-SCPM case in

the middle third of the boundary layer. Shear production for the SCPM-M cases was higher than that for the No-SCPM case near the surface up to 35 m. Beyond this height, it decreased until it attained a value equal to the No-SCPM case at 200 m. Near the inversion layer, the shear production term in the SCPM-M case increased again due to entrainment-induced motions. The implementation of perturbations also impacted TKE redistribution through turbulent transport and pressure correlation terms. Our findings suggest that momentum perturbation enhances the coupling between shear and buoyancy-driven turbulence under unstable conditions.

Applying perturbations above the CBL height generated spurious turbulent structures attributed to additional entrainment at the top of the boundary layer, near the inversion layer. On the other hand, applying SCPM-M within the boundary layer or between the CBL height and the surface layer reduces additional entertainment-induced motions and computational costs. Based on the cases studied here, it can be concluded that applying momentum perturbations up to half the CBL height (the Ktop34H case) is optimal. This is because the Ktop34H case was characterized by significant fetch reduction and minimum generation of additional turbulent motions at the inversion layer.

The application of momentum perturbations to generate turbulence in boundary-coupled LES simulations can benefit a number of disciplines and applications, including but not limited to wind energy generation, wildfire modeling, cloud-top boundary layer research (applicable to offshore wind), and dispersion problems. Accurate turbulence representation is also important for Uncrewed Aerial Vehicle research and weather forecasting. The results of this work will benefit these applications leading to an improved understanding of the physical Earth system models.

Acknowledgements

Funding for this work was provided by the U.S. DOE Office of Energy Efficiency and Renewable Energy Wind Energy Technologies Office. M. Kumar acknowledges funding support from the Dean's Dissertation Fellowship award from the Henry Samueli School of Engineering at the University of California Irvine, and the Research Applications Laboratory visitor grant from the National Center for Atmospheric Research (NCAR). M. Kumar and T. Banerjee acknowledge support from the Subcontract agreement with Los Alamos National Laboratory, subcontract no. 596883, agreement no. 351438. Banerjee is supported by the US National Science Foundation (*NSF-AGS-PDM-2146520*, *NSF-OISE-2114740*, *NSF-CPS-2209695*, *NSF-ECO-CBET-2318718*, and *NSF-DMS-2335847*), the University of California Office of the President (UCOP-LFR-20-653572), NASA (*80NSSC22K1911*), and the United States Department of Agriculture (*NIFA*

2021-67022-35908, and *USDA-20-CR-11242306-072*). The contribution of Branko Kosović was supported by the National Center for Atmospheric Research, which is a major facility sponsored by the National Science Foundation under Cooperative Agreement No. 1852977. William Lassman's and Jeffrey D. Mirocha's contributions were performed under the auspices of the U.S. Department of Energy by Lawrence Livermore National Laboratory under Contract DE-AC52-07NA27344. This research used resources provided by the Los Alamos National Laboratory Institutional Computing Program, which is supported by the U.S. Department of Energy National Nuclear Security Administration under Contract DE-AC52-06NA25396.

Author Contributions

Mukesh Kumar: Conceptualization, Methodology, Software, Data curation, Writing- Original draft preparation, Visualization, Investigation, Software, Validation, Reviewing and Editing; **Alex Jonko:** Conceptualization, Supervision, Methodology, Investigation, Validation, Supervision, Reviewing and Editing, Project administration; **William Lassman:** Investigation, Reviewing and Editing; **Jeff Mirocha:** Software, Reviewing and Editing; **Branko Kosović:** Investigation, Reviewing and Editing; **Tirtha Banerjee:** Conceptualization, Supervision, Reviewing and Editing, Project administration, Funding acquisition.

Conflicts of Interest

The authors declare no conflict of interest.

Open Research

The simulations used in this study are performed using the latest release of the WRF (v4.1.3) model (https://github.com/wrf-model/WRF).

References

J. Ching, R. Rotunno, M. LeMone, A. Martilli, B. Kosovic, P. Jimenez, and J. Dudhia. Convectively induced secondary circulations in fine-grid mesoscale numerical weather prediction models. *Monthly Weather Review*, 142(9):3284–3302, 2014.

A. Connolly, L. van Veen, J. Neher, B. J. Geurts, J. Mirocha, and F. K. Chow. Efficacy of the cell perturbation method in large-eddy simulations of boundary layer flow over complex terrain. *Atmosphere*, 12(1):55, 2021.

J. W. Deardorff. Numerical investigation of neutral and unstable planetary boundary layers. *Journal of Atmospheric Sciences*, 29(1):91–115, 1972.

J. W. Deardorff. Stratocumulus-capped mixed layers derived from a three-dimensional model. *Boundary-layer meteorology*, 18:495–527, 1980.

L. Di Mare, M. Klein, W. Jones, and J. Janicka. Synthetic turbulence inflow conditions for large-eddy simulation. *Physics of Fluids*, 18(2):025107, 2006.

I. D.-R. dos Santos and N. Yaghoobian. Effects of urban boundary layer turbulence on firebrand transport. *Fire Safety Journal*, 135:103726, 2023.

P. Giani, M. G. Genton, and P. Crippa. Modeling the convective boundary layer in the terra incognita: Evaluation of different strategies with real-case simulations. *Monthly Weather Review*, 150(5):981–1001, 2022.

S. Haupt, L. K. Berg, A. Decastro, D. J. Gagne, P. Jimenez, T. Juliano, B. Kosovic, J. D. Mirocha, E. Quon, J. Sauer, et al. Report of the atmosphere to electrons mesoscale-to-microscale coupling project (fy2019). Technical report, Pacific Northwest National Lab.(PNNL), Richland, WA (United States ..., 2019a.

S. E. Haupt, B. Kosovic, W. Shaw, L. K. Berg, M. Churchfield, J. Cline, C. Draxl, B. Ennis, E. Koo, R. Kotamarthi, et al. On bridging a modeling scale gap: Mesoscale to microscale coupling for wind energy. *Bulletin of the American Meteorological Society*, 100(12):2533–2550, 2019b.

S. E. Haupt, R. Arthur, A. Decastro, D. J. Gagne, A. Jonko, B. Kosovic, T. Mccandless, R. K. Rai, L. K. Berg, S. Dettling, et al. Fy 2020 report of the atmosphere to electrons land-based mesoscale-to-microscale coupling project. Technical report, Pacific Northwest National Lab.(PNNL), Richland, WA (United States), 2020.

S.-Y. Hong, Y. Noh, and J. Dudhia. A new vertical diffusion package with an explicit treatment of entrainment processes. *Monthly weather review*, 134(9):2318–2341, 2006.

M. Jähn, D. Muñoz-Esparza, F. Chouza, O. Reitebuch, O. Knoth, M. Haarig, and A. Ansmann. Investigations of boundary layer structure, cloud characteristics and vertical mixing of aerosols at barbados with large eddy simulations. *Atmospheric Chemistry and Physics*, 16(2):651–674, 2016.

P. A. Jiménez, J. Dudhia, J. F. González-Rouco, J. Navarro, J. P. Montávez, and E. García-Bustamante. A revised scheme for the wrf surface layer formulation. *Monthly weather review*, 140(3):898–918, 2012.

A. Keat, U. Piomelli, E. Ballaras, and H. Kaltenbach. A priori and a posteriori tests of inflow conditions for large-eddy simulations. *Phys. Fluids*, 16:4696–4712, 2004.

M. Klein, A. Sadiki, and J. Janicka. A digital filter based generation of inflow data for spatially developing direct numerical or large eddy simulations. *Journal of computational Physics*, 186 (2):652–665, 2003.

B. Kosović. Subgrid-scale modelling for the large-eddy simulation of high-reynolds-number boundary layers. *Journal of Fluid Mechanics*, 336:151–182, 1997.

M. Kumar. *Mapping and Modeling of Fires in the Wildland-Urban Interface*. University of California, Irvine, 2022.

M. Kumar, T. Banerjee, A. Jonko, J. Mirocha, and W. Lassman. Assessing the turbulence kinetic energy budget in the boundary layer using wrf-les: Impact of momentum perturbation. In *EGU General Assembly Conference Abstracts*, pages EGU21–13794, 2021.

M. Kumar, M. Frediani, T. W. Juliano, B. Kosovic, J. T. Randerson, and T. Banerjee. The role of fire-induced turbulence on ember transport. In *AGU Fall Meeting Abstracts*, volume 2022, pages A25F–1784, 2022.

M. Kumar, B. Kosovic, H. Nayak, W. Porter, J. Randerson, and T. Banerjee. Evaluating the performance of wrf in simulating winds and surface meteorology during a southern california wildfire event. *Frontiers in Earth Science*, 11:1305124, 2024.

H. Le, P. Moin, and J. Kim. Direct numerical simulation of turbulent flow over a backward-facing step. *Journal of fluid mechanics*, 330:349–374, 1997.

675 Y. Liu, T. Warner, Y. Liu, C. Vincent, W. Wu, B. Mahoney, S. Swerdlin, K. Parks, and J. Boehn-
676 ert. Simultaneous nested modeling from the synoptic scale to the les scale for wind energy
677 applications. *Journal of Wind Engineering and Industrial Aerodynamics*, 99(4):308–319, 2011.

678 L. Mazzaro, E. Koo, D. Muñoz-Esparza, J. Lundquist, and R. Linn. Random force perturba-
679 tions: A new extension of the cell perturbation method for turbulence generation in multiscale
680 atmospheric boundary layer simulations. *Journal of Advances in Modeling Earth Systems*, 11
681 (7):2311–2329, 2019.

682 L. J. Mazzaro, D. Muñoz-Esparza, J. K. Lundquist, and R. R. Linn. Nested mesoscale-to-
683 les modeling of the atmospheric boundary layer in the presence of under-resolved convective
684 structures. *Journal of Advances in Modeling Earth Systems*, 9(4):1795–1810, 2017.

685 J. Mirocha, J. Lundquist, and B. Kosović. Implementation of a nonlinear subfilter turbulence
686 stress model for large-eddy simulation in the advanced research wrf model. *Monthly Weather*
687 *Review*, 138(11):4212–4228, 2010.

688 J. Mirocha, B. Kosović, and G. Kirkil. Resolved turbulence characteristics in large-eddy simula-
689 tions nested within mesoscale simulations using the weather research and forecasting model.
690 *Monthly Weather Review*, 142(2):806–831, 2014.

691 C.-H. Moeng and P. P. Sullivan. A comparison of shear-and buoyancy-driven planetary boundary
692 layer flows. *Journal of Atmospheric Sciences*, 51(7):999–1022, 1994.

693 C.-H. Moeng and J. C. Wyngaard. Statistics of conservative scalars in the convective boundary
694 layer. *Journal of Atmospheric Sciences*, 41(21):3161–3169, 1984.

695 A. S. Monin and A. M. Obukhov. Basic laws of turbulent mixing in the surface layer of the
696 atmosphere. *Contrib. Geophys. Inst. Acad. Sci. USSR*, 151(163):e187, 1954.

697 D. Muñoz-Esparza and B. Kosović. Generation of inflow turbulence in large-eddy simulations of
698 nonneutral atmospheric boundary layers with the cell perturbation method. *Monthly Weather*
699 *Review*, 146(6):1889–1909, 2018.

700 D. Muñoz-Esparza, B. Kosović, C. García-Sánchez, and J. Van Beeck. Nesting turbulence in an
701 offshore convective boundary layer using large-eddy simulations. *Boundary-layer meteorology*,
702 151:453–478, 2014a.

D. Muñoz-Esparza, B. Kosović, J. Mirocha, and J. van Beeck. Bridging the transition from mesoscale to microscale turbulence in numerical weather prediction models. *Boundary-layer meteorology*, 153(3):409–440, 2014b.

D. Muñoz-Esparza, B. Kosović, J. Van Beeck, and J. Mirocha. A stochastic perturbation method to generate inflow turbulence in large-eddy simulation models: Application to neutrally stratified atmospheric boundary layers. *Physics of Fluids*, 27(3):035102, 2015.

D. Muñoz-Esparza, J. A. Sauer, R. R. Linn, and B. Kosović. Limitations of one-dimensional mesoscale pbl parameterizations in reproducing mountain-wave flows. *Journal of the Atmospheric Sciences*, 73(7):2603–2614, 2016.

D. Muñoz-Esparza, J. K. Lundquist, J. A. Sauer, B. Kosović, and R. R. Linn. Coupled mesoscale-les modeling of a diurnal cycle during the cwex-13 field campaign: From weather to boundary-layer eddies. *Journal of Advances in Modeling Earth Systems*, 9(3):1572–1594, 2017.

M. Pamiès, P.-E. Weiss, E. Garnier, S. Deck, and P. Sagaut. Generation of synthetic turbulent inflow data for large eddy simulation of spatially evolving wall-bounded flows. *Physics of fluids*, 21(4):045103, 2009.

R. K. Rai, L. K. Berg, B. Kosović, J. D. Mirocha, M. S. Pekour, and W. J. Shaw. Comparison of measured and numerically simulated turbulence statistics in a convective boundary layer over complex terrain. *Boundary-Layer Meteorology*, 163:69–89, 2017a.

R. K. Rai, L. K. Berg, M. Pekour, W. J. Shaw, B. Kosovic, J. D. Mirocha, and B. L. Ennis. Spatiotemporal variability of turbulence kinetic energy budgets in the convective boundary layer over both simple and complex terrain. *Journal of Applied Meteorology and Climatology*, 56(12):3285–3302, 2017b.

J. A. Sauer, D. Muñoz-Esparza, J. M. Canfield, K. R. Costigan, R. R. Linn, and Y.-J. Kim. A large-eddy simulation study of atmospheric boundary layer influence on stratified flows over terrain. *Journal of the Atmospheric Sciences*, 73(7):2615–2632, 2016.

W. C. Skamarock, J. B. Klemp, J. Dudhia, D. O. Gill, Z. Liu, J. Berner, W. Wang, J. G. Powers, M. G. Duda, D. M. Barker, et al. A description of the advanced research wrf model version 4. *National Center for Atmospheric Research: Boulder, CO, USA*, 145:145, 2019.

731 C. M. Smith and E. D. Skyllingstad. Investigation of upstream boundary layer influence on
732 mountain wave breaking and lee wave rotors using a large-eddy simulation. *Journal of the*
733 *Atmospheric Sciences*, 66(10):3147–3164, 2009.

734 A. Spille-Kohoff and H.-J. Kaltenbach. Generation of turbulent inflow data with a pre-
735 scribed shear-stress profile. Technical report, TECHNISCHE UNIV BERLIN (GERMANY)
736 HERMANN-FOTTINGER INST FUR STROMUNGSMECHANIK, 2001.

737 R. B. Stull. *An introduction to boundary layer meteorology*, volume 13. Springer Science &
738 Business Media, 1988.

739 G. R. Tabor and M. Baba-Ahmadi. Inlet conditions for large eddy simulation: A review. *Com-*
740 *puters & Fluids*, 39(4):553–567, 2010.

741 C. Talbot, E. Bou-Zeid, and J. Smith. Nested mesoscale large-eddy simulations with wrf: Per-
742 formance in real test cases. *Journal of Hydrometeorology*, 13(5):1421–1441, 2012.

743 Z.-T. Xie and I. P. Castro. Efficient generation of inflow conditions for large eddy simulation of
744 street-scale flows. *Flow, turbulence and combustion*, 81(3):449–470, 2008.

745 F. J. Zajaczkowski, S. E. Haupt, and K. J. Schmehl. A preliminary study of assimilating numerical
746 weather prediction data into computational fluid dynamics models for wind prediction. *Journal*
747 *of Wind Engineering and Industrial Aerodynamics*, 99(4):320–329, 2011.

748 J. Zhong, X. Cai, and Z.-T. Xie. Implementation of a synthetic inflow turbulence generator in
749 idealised wrf v3. 6.1 large eddy simulations under neutral atmospheric conditions. *Geoscientific*
750 *Model Development*, 14(1):323–336, 2021.

751 B. Zhou and F. K. Chow. Nighttime turbulent events in a steep valley: A nested large-eddy
752 simulation study. *Journal of the Atmospheric Sciences*, 70(10):3262–3276, 2013.

5 Supplementary Materials

5.1 Effects of the spatial averaging domain

Heat flux ($\overline{w'\theta'}$) profiles are not similar in all the cases when we apply SCPM-M with higher amplitudes of forces. As it is shown in Figure 8(a and b), the Ktop34H starts diverging from other SCPM-M cases at 75 m and continued to do so all the way to the inversion layer. Also, the Ktop34H produces highest entrainment (around 27 kKms^{-1}) at the capping inversion (600 m) as compared to Ktop54H, Ktop88H, and No-SCPM. Heat fluxes ($\overline{w'\theta'}$) are the same up to the inversion layer (600 m) for all the simulations with lower and medium amplitude SCPM-M cases (Figure 8(b)). At the inversion layer, entrainment is highest (around 25 kKms^{-1}) for the Ktop88H, and the same hold true for the Ktop54H (Figure 8(a)). In the case of Ktop34H, when we apply SCPM-M at the half of the boundary layer (303 m), entrainment is higher (around 20 kKms^{-1}) than the Ktop54H and Ktop88H, but lower than the No-SCPM. However, heat fluxes ($\overline{w'\theta'}$) from the surface up to 200 m are almost equal in all the lower amplitude SCPM-M cases. Therefore, comparing Figure 8(a) and Figure 8(b), SCPM-M applied with higher forcing amplitudes below the boundary layer (Ktop34H) produces the highest heat flux ($\overline{w'\theta'}$) and is suitable for several applications.

Similar to the heat flux ($\overline{w'\theta'}$) profiles, we compute the momentum flux ($\overline{u'w'}$) profiles as shown in Figure 8(c and d) for the different simulations. The momentum flux ($\overline{u'w'}$), a flow property, is lost to the ground in the boundary layer and therefore, is negative in the boundary layer in all cases (Stull, 1988) of the simulations. Consequently, when momentum flux is multiplied by a negative sign, results in a positive contribution to the variance and TKE. Figure 8(c) shows that when we apply higher amplitude momentum perturbation near the CBL (Ktop54H) or below it (Ktop34H), produces a higher momentum flux ($\overline{u'w'}$) as compared to the case where SCPM-M was applied above the CBL (Ktop88H). Therefore, the turbulent motions are generated and significantly better resolved when SCPM-M is applied within the CBL. However, in the case of No-SCPM, we observe the highest momentum flux ($\overline{u'w'}$) within 200 m. This was due to the way we performed area averaging in these profiles. More specifically, it is also because of the fact that No-SCPM is unable to capture turbulence generation at the beginning of the inflow boundary and create a fetch while generating extra turbulence afterward (above x values of around 6,000 m). Since we are taking the area average over that specific value over the x axis (6,000 m to the end of the domain), it is expected that we would observe a large momentum flux ($\overline{u'w'}$). In addition, on comparing Figure 8(c) and Figure 8(d) while we implement SCPM-M with

higher and lower amplitudes, we observe that at the lower and medium amplitudes, SCPM-M produces similar profiles of momentum flux ($\overline{u'w'}$) in the CBL (8(d)). At the higher amplitudes, the SCPM-M generates slightly different momentum fluxes ($\overline{u'w'}$) especially when closer to the surface layer (i.e., up to 200 m). We also find that the Ktop34H loses the maximum momentum flux (negative) as compared to the Ktop54H and Ktop88H. Therefore, we can observe that applying SCPM-M with a higher amplitude below the CBL produces turbulence structures that could sufficiently represent the flow characteristics in the CBL up to 200 m.

We find that the No-SCPM generates extra TKE in the up to 200 m (3a-b) as it produces additional variances and turbulence structures through momentum fluxes ($\overline{u'w'}$) as discussed previously. Furthermore, it starts decreasing above 200 m, and its value is decreased by 60% from 200 m to 400 m. It reaches close to zero at 800 m. In addition, it crosses all the SCPM-M cases at 200 m and decreases at the highest rate as compared to all of the other cases (S13c-d).

Furthermore, we find that TKE is different in Ktop34H, Ktop54H, and Ktop88H up to 350 m. In addition, we observe that the Ktop34H produces the highest TKE while the Ktop88H produces the lowest TKE, and Ktop54H generates the TKE that is somewhere between Ktop34H and Ktop88H (S13c). The value of TKE for Ktop34H decreases at a lower rate as compared with the No-SCPM case and it decreases by 60% from 200 m to 600 m (near the inversion layer). Its value decreases at a faster rate above 600 m and it decreases to close to zero at the different heights in the chosen cases of SCPM-M. For instance, it decreases to zero at around 900 m for Ktop34H, while reaches zero at 1,100 m and 1,300 m for Ktop54H and Ktop88H respectively (S13c). On the other hand, in the case of SCPM-M with lower amplitudes, a practically equivalent TKE is generated up to 150 m (S13b). Also, from 200 m to 600 m (i.e., within the boundary layer), Ktop34L, Ktop54L, Ktop88L, and Ktop88M dominate the magnitude of TKE generation (S13d). Furthermore, while observing the TKE profiles above the inversion layer (600 m), we find that the TKE decreases sharply just after 600 m and its value reaches zero at 800 m for all the cases (S13d).

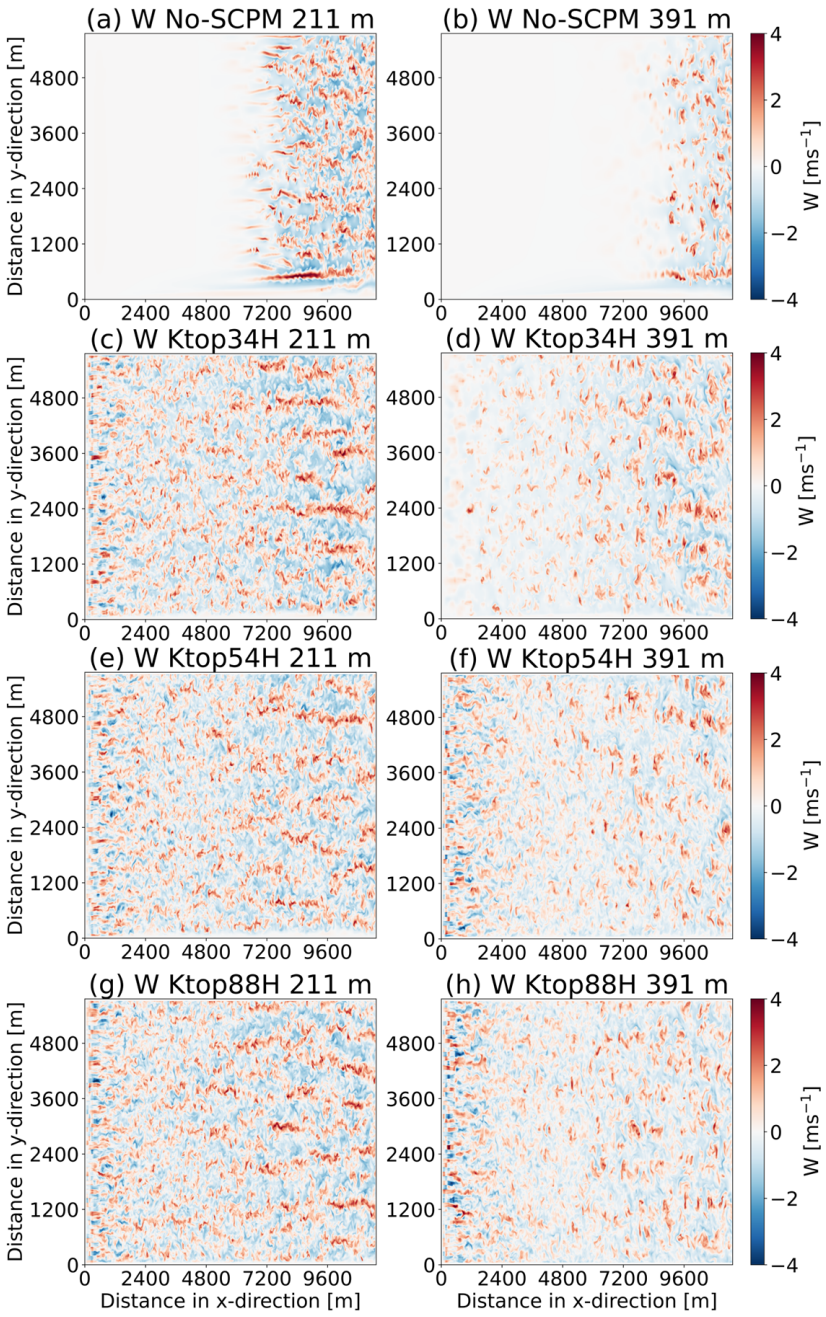

Figure S12: W component of velocities (ms^{-1}) at two different heights that is at half (level=27, z=211 m) and at two-third (level=37, z=391 m) of the boundary layer height for (a-b) No-SCPM, (c-d) Ktop54H (e-f) Ktop54H (g-h) Ktop88H. The color bar corresponds to the velocity for panels (a) to (h). The domain shown is the inner LES domain used in this study.

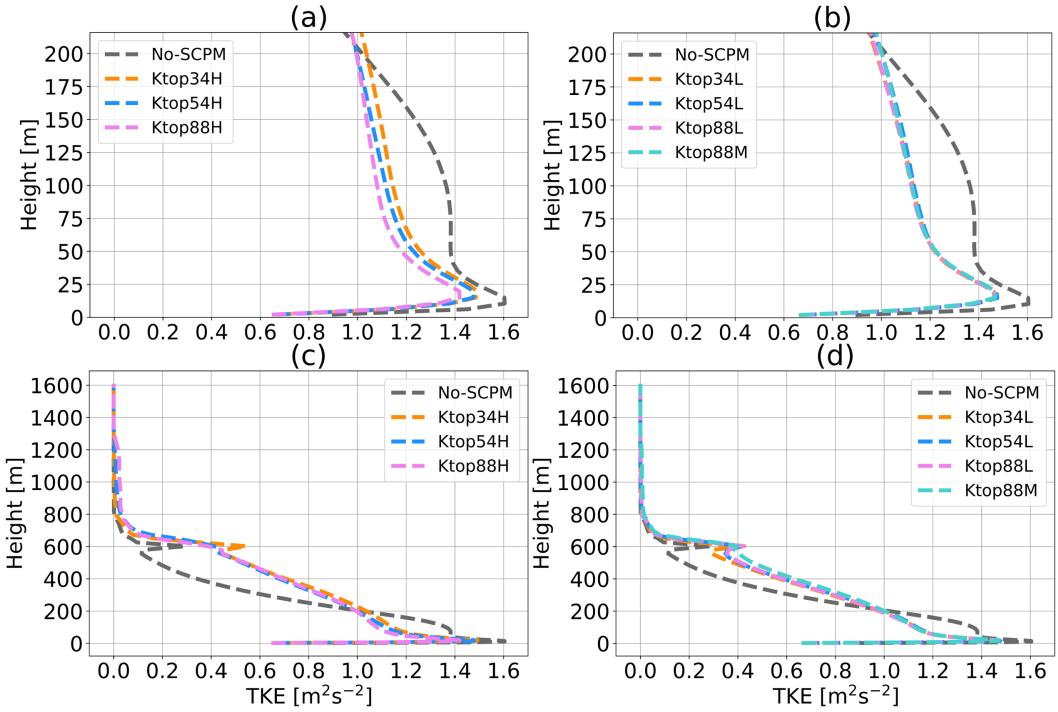

Figure S13: Turbulence kinetic energy (TKE) profile after applying momentum perturbation with higher amplitude (Table 1) in the right panels and lower & medium amplitudes in the left panels respectively. These profiles are generated for TKE that are area-averaged over the last three-quarters of the domain, i.e., all y and x from 2,880 m to 11,520 m with (a) high amplitude SCPM-M up to 216 m, (b) low and medium amplitude SCPM-M up to 216 m, (c) high amplitude SCPM-M up to the top of the inner domain, and (d) low and medium amplitude SCPM-M up to the top the inner domain.

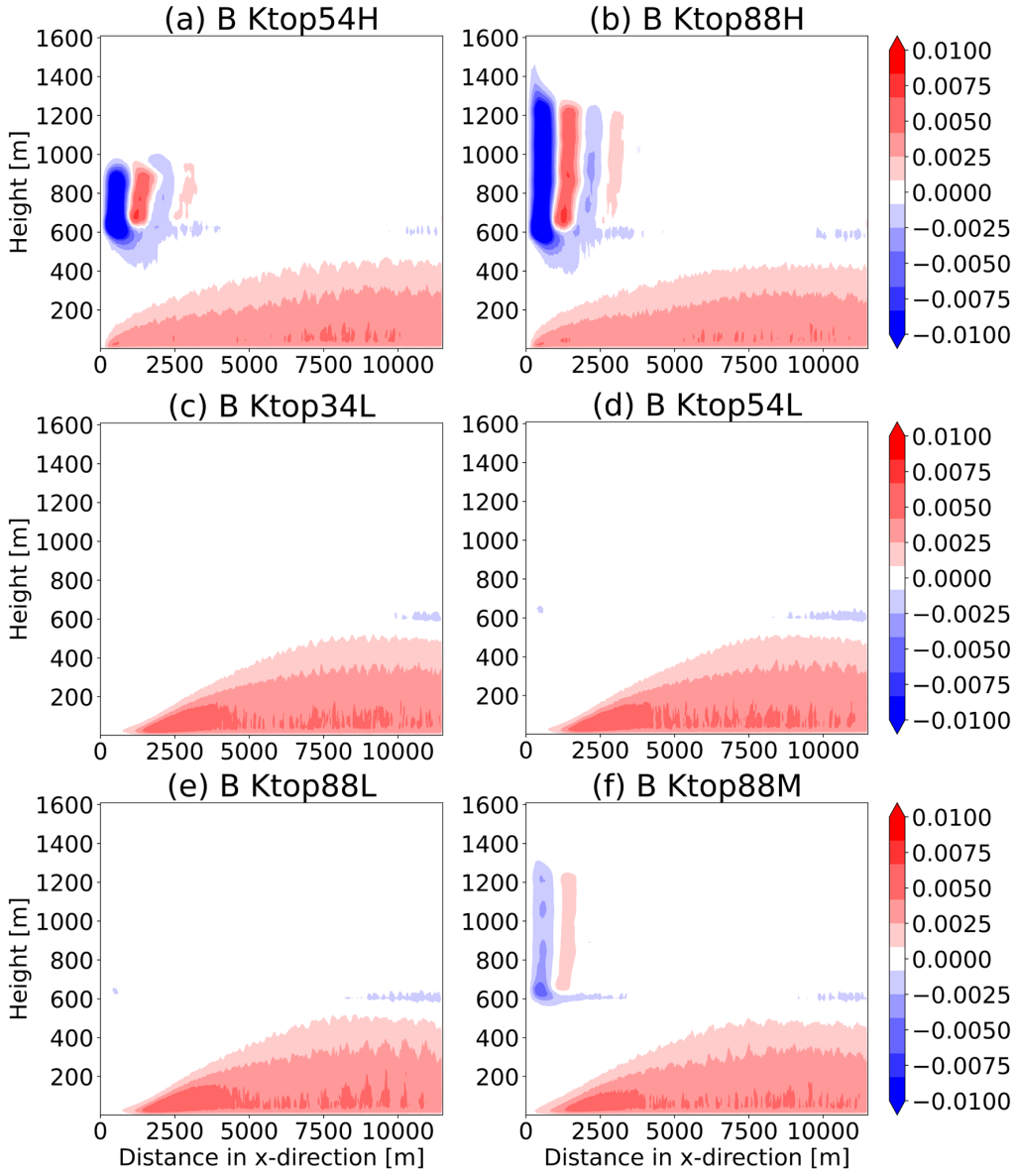

Figure S14: Y averaged buoyancy term after applying momentum perturbation with higher amplitudes (Table 1) with (a) Ktop54H, (b) Ktop88H, (c) Ktop34L, (d) Ktop54L, (e) Ktop88L, and (f) Ktop88M. The color bar corresponds to the magnitude of the buoyancy term for panels (a) to (f). These plots are generated for buoyancy terms that are Y-averaged over the entire inner domain.

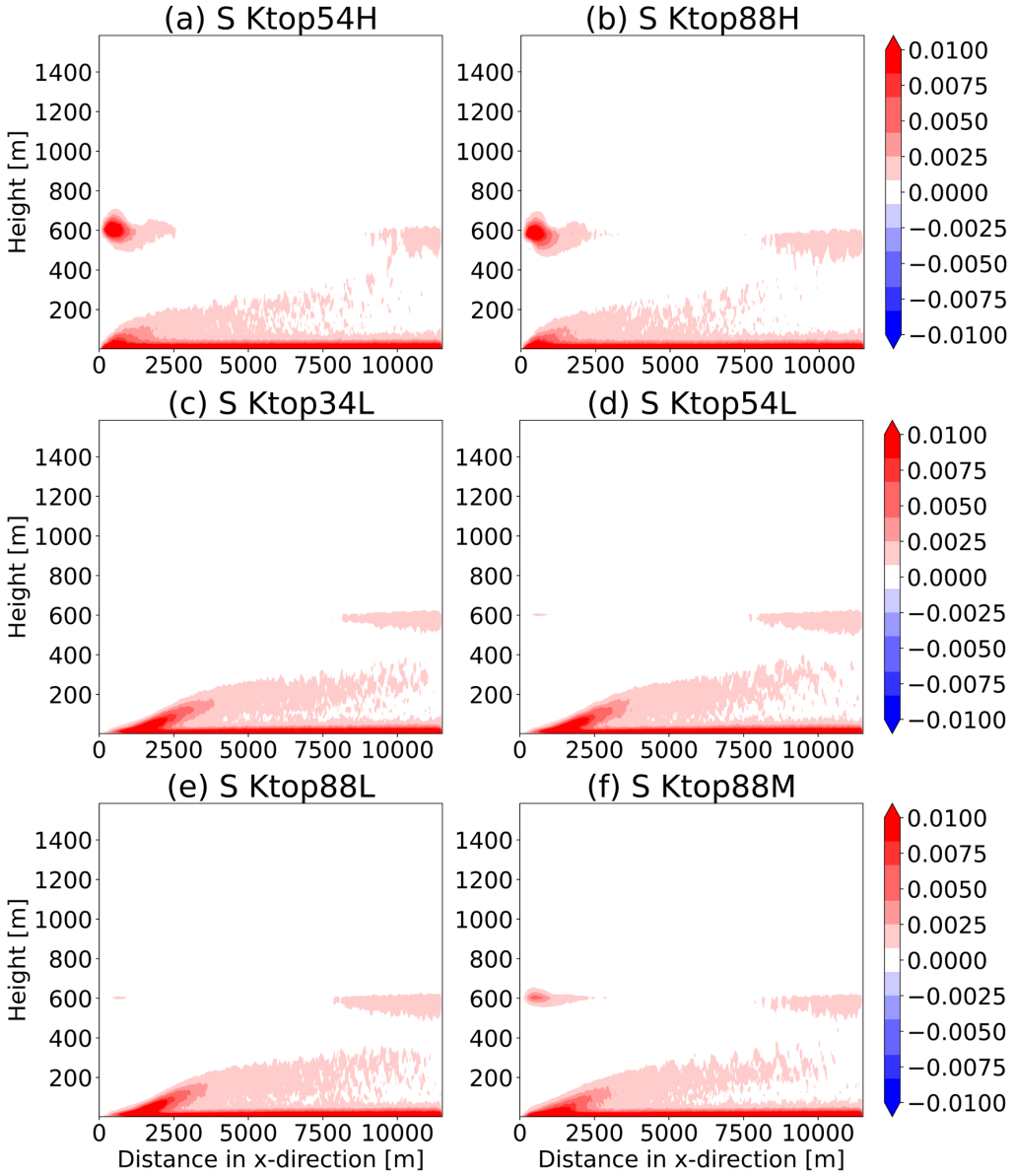

Figure S15: Y averaged shear term after applying momentum perturbation with higher amplitudes (Table 1) with (a) Ktop54H, (b) Ktop88H, (c) Ktop34L, (d) Ktop54L, (e) Ktop88L, and (f) Ktop88M. The color bar corresponds to the magnitude of the shear term for panels (a) to (f). These plots are generated for shear terms that are Y-averaged over the entire inner domain.

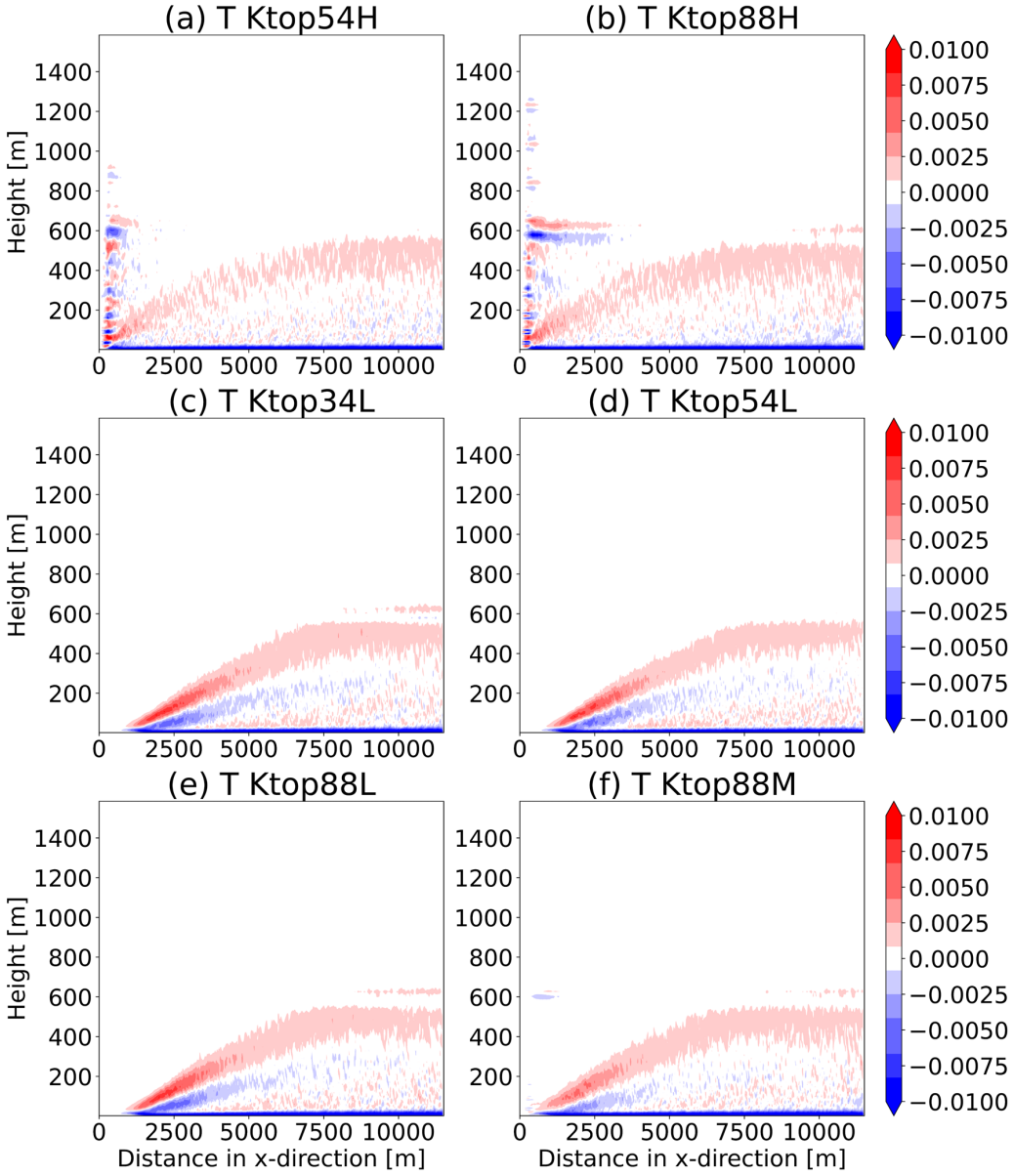

Figure S16: Y averaged transport term after applying momentum perturbation with higher amplitudes (Table 1) with (a) Ktop54H, (b) Ktop88H, (c) Ktop34L, (d) Ktop54L, (e) Ktop88L, and (f) Ktop88M. The color bar corresponds to the magnitude of transport term for panels (a) to (f). These plots are generated for transport terms that are Y-averaged over the entire inner domain.

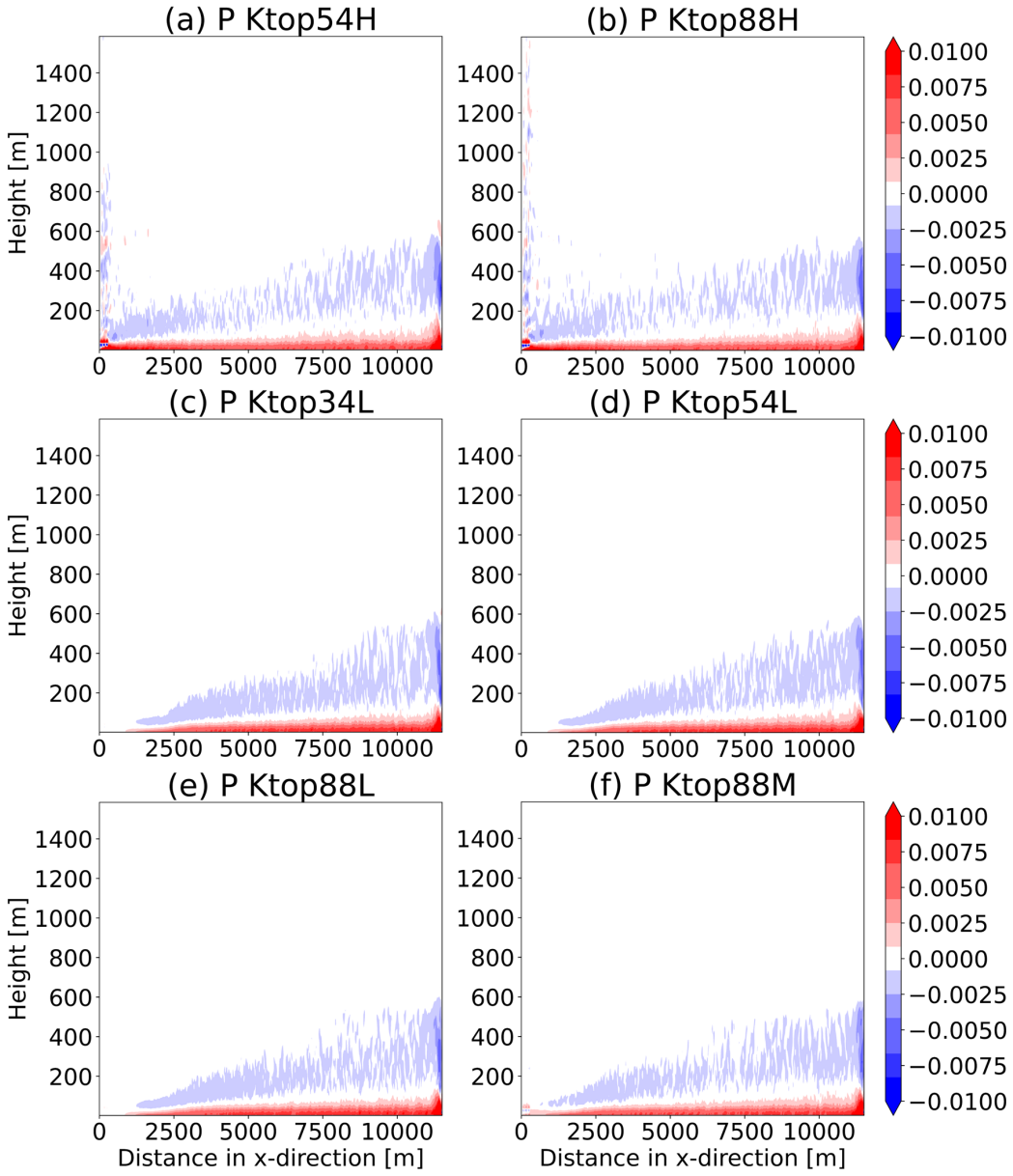

Figure S17: Y averaged pressure correlation term after applying momentum perturbation with higher amplitudes (Table 1) with (a) Ktop54H, (b) Ktop88H, (c) Ktop34L, (d) Ktop54L, (e) Ktop88L, and (f) Ktop88M. The color bar corresponds to the magnitude of the pressure correlation term for panels (a) to (f). These plots are generated for pressure correlation terms that are Y-averaged over the entire inner domain.

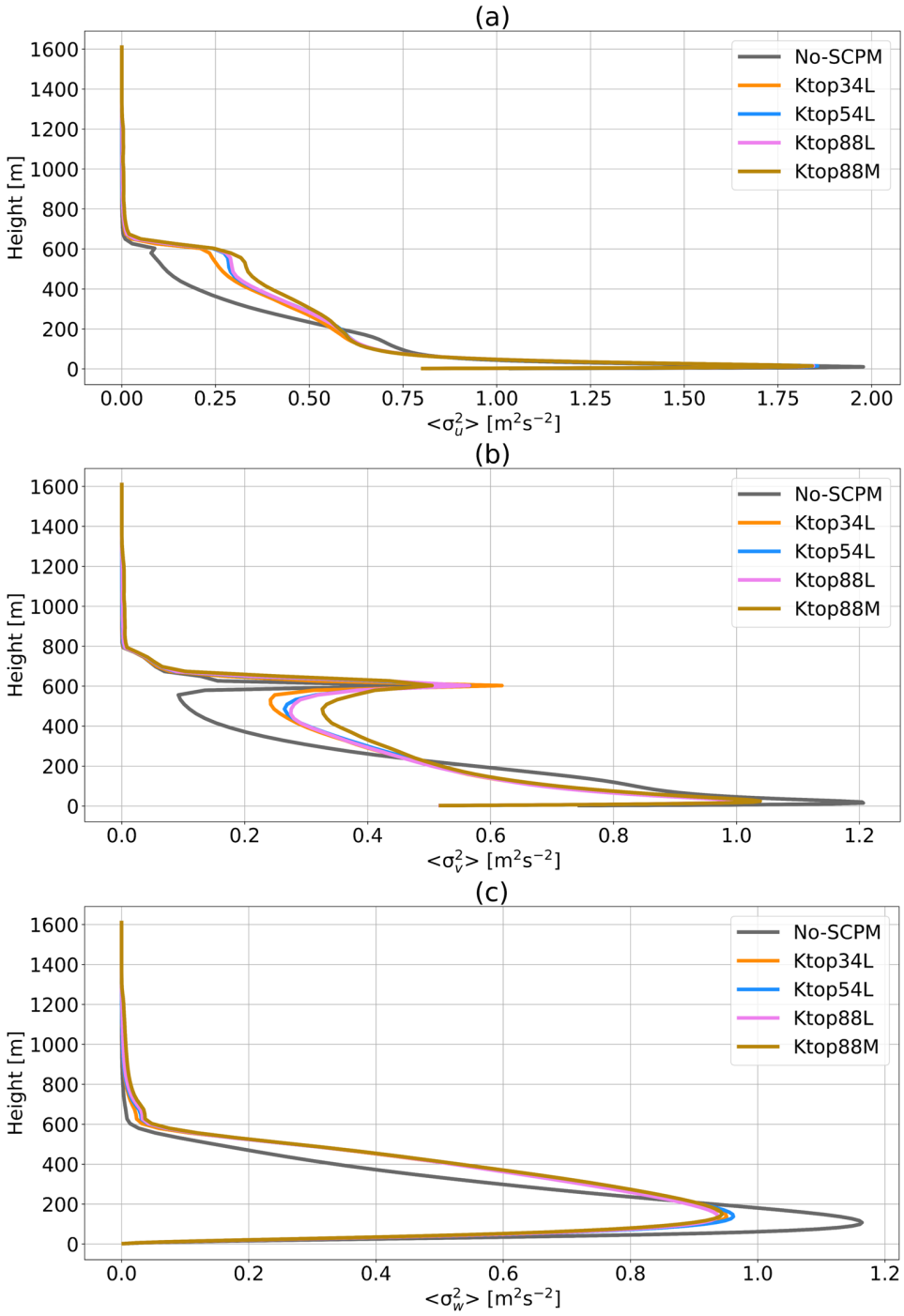

Figure S18: XY-averaged (a) σ_u^2, (b) σ_v^2, and (c) σ_w^2 for all the cases shown in Table 1 for No-SCPM, lower, and medium amplitude simulations i.e., No-SCPM, Ktop34L, Ktop54L, Ktop88L, & Ktop88M. These results are shown from the last simulation period at 20 Z.